

1       **Variation in the Pedersen Conductance near Jupiter’s**  
2       **Main Emission Aurora: Comparison of Hubble Space**  
3       **Telescope and Galileo Measurements**

4       **M. J. Rutala<sup>1,2</sup>, J. T. Clarke<sup>2</sup>, M. F. Vogt<sup>2</sup>, and J. D. Nichols<sup>3</sup>**

5       <sup>1</sup>School of Cosmic Physics, DIAS Dunsink Observatory, Dublin Institute for Advanced Studies, Dublin 15,  
6       Ireland

7       <sup>2</sup>Center for Space Physics, Boston University, Boston MA

8       <sup>3</sup>Department of Physics and Astronomy, University of Leicester, Leicester UK

9       **Key Points:**

- 10       • The effective ionospheric Pedersen conductance in Jupiter’s main emission auro-  
11       ral region is derived from remote and in-situ measurements.
- 12       • Effective Pedersen conductances of  $\sim 0.14$  mho and field-aligned auroral currents  
13       near  $\sim 10$  MA  $\text{rad}^{-1}$  are derived, consistent with past work.
- 14       • The effective Pedersen conductance varies significantly in magnetic local time, and  
15       may explain the enigmatic motions of some auroral forms.

---

Corresponding author: M. J. Rutala, [mrutala@cp.dias.ie](mailto:mrutala@cp.dias.ie)

**Abstract**

We present the first large-scale statistical survey of the Jovian main emission (ME) to map auroral properties from their ionospheric locations out into the equatorial plane of the magnetosphere, where they are compared directly to in-situ spacecraft measurements. We use magnetosphere-ionosphere (MI) coupling theory to calculate currents from the auroral brightness as measured with the Hubble Space Telescope and from plasma flow speeds measured in-situ with the *Galileo* spacecraft. The effective Pedersen conductance of the ionosphere ( $\Sigma_P^*$ ) remains a free parameter in this comparison. We calculate the Pedersen conductance from the combined datasets, and find it ranges from  $0.03 < \Sigma_P^* < 2.40$  mho overall with averages of  $0.13_{-0.07}^{+0.26}$  mho in the north and  $0.16_{-0.10}^{+0.34}$  mho in the south. Considering the HST-derived field-aligned currents per radian of azimuth only, we find values of  $I_{\parallel} = 9.34_{-3.54}^{+5.72}$  MA rad<sup>-1</sup> and  $I_{\parallel} = 8.61_{-3.05}^{+6.77}$  MA rad<sup>-1</sup> in the north and south, respectively, in general agreement with previous results. Taking the currents and effective Pedersen conductance together, we find that the average ME intensity and plasma flow speed in the middle magnetosphere (10-30  $R_J$ ) are broadly consistent with one another under MI coupling theory. We find evidence for peaks in the distribution of  $\Sigma_P^*$  near dawn, then again near 12 and 14 hours magnetic local time (MLT). This variation in Pedersen conductance with MLT may indicate the importance of conductance in modulating MLT- and local-time-asymmetries in the ME, including the apparent sub-rotation of some auroral features within the ME.

**Plain Language Summary**

The brightest part of Jupiter’s aurorae– the main emission– forms arcs of sheet-like lights surrounding both magnetic poles, similar to the Earth’s aurorae. At both planets, these lights are caused by charged particles flowing into the planet’s atmosphere, where they collide with gases and glow. According to one theory, at Jupiter these particles are electrons which flow in electrical currents connecting the planet to the charged-particle-filled space surrounding it. Here, we use Hubble Space Telescope images of Jupiter’s aurorae spanning a decade to build up an average picture of the brightness and location of this main emission. The brightness is related to the energy of the electrons, which in turn is related to the strength of the electrical currents. We then use particle measurements made by the *Galileo* spacecraft in orbit around Jupiter to make an average picture of these particles as they move around Jupiter. These speeds are related to the same electrical currents, but include an electrical conductivity term describing how easily currents flow through Jupiter’s auroral atmosphere. We combine all these measurements to calculate the conductivity, and present results which are consistent with expectations but which fluctuate more quickly than expected in parts of the main emission.

**1 Introduction**

Jupiter’s ultraviolet (UV) auroral main emission (ME), typically the most powerful component of the planet’s large-scale auroral regions, takes the form of a partially-closed oval of auroral emission surrounding each of the planet’s magnetic poles. The Jovian aurorae are detectable at all local times (LT) including on the planet’s dayside (Clarke et al., 2004; Bonfond et al., 2017), where they are significantly brighter than the reflected solar UV at Jupiter (Gustin et al., 2012) and can thus be observed routinely with the Hubble Space Telescope (HST). In the southern hemisphere, the ME forms a nearly circular curtain of light; however, the presence of multiple significant non-dipolar magnetic field components in the northern hemisphere complicates the ME structure, resulting in a characteristic ‘kidney bean’ shape offset from the rotational pole (Grodent et al., 2008; Connerney et al., 2022), as shown by the HST observation and statistically-averaged reference main oval (‘statistical main oval’, or SMO, from Nichols et al. (2009)) in Figure 1a.

66 The ME has historically been thought to originate from the magnetosphere-ionosphere  
67 (MI) coupling currents flowing in the Jovian middle magnetosphere, radially outward in  
68 the equatorial plasma disc, equatorward in the ionosphere, and along magnetic field lines  
69 between (Hill, 2001; Cowley & Bunce, 2001; Nichols & Cowley, 2003, 2004, 2005; Ray  
70 et al., 2010, 2014; Smith & Aylward, 2009; Tao et al., 2009). This current system arises  
71 from the azimuthal distortion (or ‘bendback’) of the field resulting from the planet’s reser-  
72 voir of angular momentum opposing the decrease in angular velocity experienced by plasma-  
73 laden flux tubes as they diffuse radially outward. In the absence of torques, these dif-  
74 fusing flux tubes would tend to conserve angular momentum, resulting in a decrease in  
75 the angular velocity proportional to  $r^{-2}$ . As the flux tubes lag behind corotation, they  
76 warp the magnetic field resulting in the azimuthal bendback of the field structure. The  
77 azimuthal component of the magnetic field now present results in a loop of field-aligned  
78 current which acts to partially enforce the corotation of the plasma within the magne-  
79 todisk by exerting a  $\mathbf{J} \times \mathbf{B}$  force in the direction of corotation. The strongest field-aligned  
80 currents occur near where rigid corotation breaks down (Hill, 1979; Nichols & Cowley,  
81 2004). The ME current system is characterized primarily by the rapid rotation and strength  
82 of Jupiter’s magnetic field, rather than by solar influence as is the case in the Earth’s  
83 own magnetosphere and auroral ovals (Cowley & Bunce, 2001; Southwood & Kivelson,  
84 2001), though solar wind influence is not completely absent (Kita et al., 2019; Nichols  
85 et al., 2017). These MI-coupling currents and the associated ME ovals are thus always  
86 present, owing to the continuous production of Iogenic plasma and diffusion of this plasma  
87 outward through the magnetosphere.

88 The production and diffusion of Iogenic plasma is not constant and the Jovian mag-  
89 netosphere varies in System III (SIII) magnetic longitude ( $\lambda_{III}$ ), local time (LT), and  
90 magnetic local time (MLT). This results in various asymmetries in the brightness, shape,  
91 distribution, and dynamics of auroral forms within the ME oval. While both hemispheres  
92 have similar total emitted UV powers, the southern ME is brighter on average than the  
93 northern (Gérard et al., 2013) and the dusk side of the ME is brighter on average than  
94 dawn, an effect which is amplified in the brighter southern hemisphere (Bonfond et al.,  
95 2015). On occasions where the dawn side is brighter than dusk, an exceptionally bright  
96 auroral feature— a dawn storm, perhaps— is typically located on the dawn ME (Gérard,  
97 Grodent, et al., 1994; Bonfond et al., 2021; Rutala et al., 2022). While the locations of  
98 the ME remain fixed in SIII longitude and latitude (Clarke et al., 2004; Gérard, Dols,  
99 et al., 1994; Grodent et al., 2003), auroral features on the ME may subcorotate, lagging  
100 behind the rigid corotation rate of the planet. Subcorotation occurs more often in the  
101 dawn sector than the noon and dusk sectors (Rutala et al., 2022), an effect which ap-  
102 pears to be separate from the appearance of bright dawn storms. Additional subcoro-  
103 tating auroral forms, the ME auroral discontinuity (Radioti et al., 2008) and small-scale  
104 brightening (Palmaerts et al., 2014) are observed localized near noon. The dusk side of  
105 the ME as viewed from the Earth is typically wider and more diffuse than near dawn  
106 (Gérard, Dols, et al., 1994); this asymmetry is larger in the northern hemisphere, where  
107 the northern magnetic anomaly is typically located in remote observations (Grodent et  
108 al., 2008). This asymmetry was originally considered to be a variation in local time (Caldwell  
109 et al., 1992), before improved HST observations made it appear to be a variation in SIII  
110 longitude (Gérard, Dols, et al., 1994). While recent *Juno* UVS observations of the po-  
111 lar aurorae have revealed considerable local time control (Greathouse et al., 2021), the  
112 relationship of this apparent dawn-dusk asymmetry in the ME to either local time or SIII  
113 longitude remains unclear.

114 These phenomena have generally been thought to arise from deviations from the  
115 ideal axisymmetric MI-coupling theory previously discussed. However, predictions of this  
116 theory are not always in accordance with observations, raising the possibility that the  
117 MI-coupling theory itself only partially describes the generation of the ME oval at Jupiter  
118 (Bonfond et al., 2020). Mean field-aligned currents of 58 MA and 24 MA in the south-  
119 ern and northern ME regions, respectively, have been derived from near-planet ( $\lesssim 2R_J$ )

120 *Juno* magnetometer (MAG) measurements of magnetic field perturbations associated  
 121 with MI-coupling currents, reflecting the observed north-south brightness asymmetry of  
 122 the ME ovals (Kotsiaros et al., 2019). These currents appear in primarily longitudinal,  
 123 though variable, sheets in keeping with the schematic picture of MI coupling theory. An  
 124 analysis of the same *Juno* orbits, but focusing on magnetic field perturbations measured  
 125 along auroral magnetic field lines at larger radial distance ( $4 - 16R_J$ ) in the northern  
 126 hemisphere, agrees that the current structure is extended in longitude and finds larger  
 127 currents of  $\sim 34$  MA in that hemisphere, somewhat reducing the north-south asymme-  
 128 try (Kamran et al., 2022). Further *Juno* measurements have found that the field lines  
 129 associated with ME aurorae host precipitating electrons, as required to drive field-aligned  
 130 currents, along with bi-directional electron distributions (Mauk et al., 2017, 2018), sug-  
 131 gesting that additional auroral emission zones, co-located or nearly co-located with the  
 132 ME, may be driven by acceleration processes other than field-aligned potentials (Mauk  
 133 et al., 2020). The measured bi-directional electron distributions may, however, be a sec-  
 134 ondary effect, driven by the flow of intense field-aligned currents (Nichols & Cowley, 2022).  
 135 The equatorial radial currents derived from *Juno* magnetometer measurements are highly  
 136 correlated with simultaneous HST observations of the dawnside ME auroral intensity (Nichols  
 137 & Cowley, 2022). On large scales and within the middle magnetosphere, the MI-coupling  
 138 theory still reproduces measurements of current structures (Kotsiaros et al., 2019; Lorch  
 139 et al., 2020; Wang et al., 2021; Al Saati et al., 2022; Kamran et al., 2022) and observa-  
 140 tions of ME auroral brightness variation, both during short-term enhancements (Nichols  
 141 et al., 2020) and solar-wind pressure enhancements (Cowley et al., 2008).

142 A further discrepancy between the modeled and observed auroral MI-coupling sys-  
 143 tem at Jupiter lies in the auroral brightness asymmetry across the dayside ME. While  
 144 the dusk side of the ME oval is typically observed to be brighter than the dawn side (Bonfond  
 145 et al., 2015), models predict that this asymmetry should be reversed owing to the larger  
 146 field bend-back in the dawn sector (Ray et al., 2014). Field bend-back is strongly cor-  
 147 related with ME auroral brightness, particularly near dawn (Nichols & Cowley, 2022).  
 148 Field bend-back is caused by angular plasma flow speeds in the middle magnetosphere  
 149 slower than the rotation rate of the planet, or subcorotation relative to the planet’s ro-  
 150 tation, so in considering only the quasi-steady-state MI coupling current system, an an-  
 151 t anticorrelation between the degree of field bend-back and plasma angular velocity is ex-  
 152 pected (Bonfond et al., 2020). A partial ring current, spanning the nightside middle mag-  
 153 netosphere with a source near dusk and a sink near dawn (Walker & Ogino, 2003) may  
 154 ease this tension if the ring current closes along field-aligned currents, decreasing the ef-  
 155 fective field-aligned currents near dawn and increasing them near dusk (Bonfond et al.,  
 156 2015). On top of this effect, careful consideration is required to relate instantaneous, in-  
 157 situ measurements of plasma velocity to the measurement of magnetic field bend-back  
 158 in a dynamic region of the magnetosphere such as the dawn sector. The anticorrelation  
 159 between field bend-back and plasma velocity is only maintained in the quasi-steady-state  
 160 scenario. If magnetospheric plasma near dawn is rapidly accelerated, the measured plasma  
 161 velocity may be high despite large degrees of field bend-back, as the plasma and field lines  
 162 have yet to “catch up” to corotational velocity. This scenario matches observations of  
 163 both the plasma (Krupp et al., 2001; Bagenal et al., 2016) and the magnetic field (Khurana  
 164 & Schwarzl, 2005) near dawn. Such a sudden acceleration of the middle magnetospheric  
 165 plasma may be driven by a sharp increase in the conductance of the MI-coupling circuit,  
 166 as is the case near the dawn terminator where the previously-unlit ionosphere is re-photoionized  
 167 by solar extreme ultraviolet (EUV) light (Tao et al., 2010). This scenario has been sug-  
 168 gested to explain the apparent subcorotation of some auroral forms relative relative to  
 169 the SMO in the dawn sector (Rutala et al., 2022), and will be explored here in more de-  
 170 tail.

171 Here, we present the first large-scale statistical survey of the typical HST-observed  
 172 ME brightness, spanning more than 10 years and 200 cumulative hours of exposure time.  
 173 The ME brightness is mapped from the polar ionosphere out into the magnetospheric

174 equatorial plane and averaged in bins defined by MLT, equatorial radial distance ( $\rho_e$ ),  
175 and the solar central meridian longitude (solar CML), so that variations relative to MLT  
176 and  $\lambda_{III}$  can be differentiated. From these binned values, the associated maximum field-  
177 aligned current density and total currents under MI-coupling theory are derived. We com-  
178 pare the derived total currents from this novel analysis of HST observations to litera-  
179 ture values, finding good agreement in scale. These values are then compared to non-  
180 contemporaneous in-situ *Galileo* Plasma Science (PLS) measurements of the plasma flow  
181 speed and associated field-aligned current density and total current binned in the same  
182 way as the HST observations in order to perform a superposed epoch analysis. Finally,  
183 we compare the HST- and *Galileo*- derived currents directly, assuming that they fully  
184 describe the large-scale, time-averaged state of the MI-coupling system, to derive a dis-  
185 tribution of the Pedersen conductance in MLT,  $\rho_e$ , and solar CML. The resulting con-  
186 ductance distribution is additionally mapped back into the ionosphere. We find that the  
187 Pedersen conductance peaks in the dawn sector, and varies primarily in MLT, consis-  
188 tent with controlling the subcorotation of auroral forms in the dawn ME and helping re-  
189 solve the tension between high degrees of field bend-back and high plasma velocities in  
190 the dawn sector.

## 191 2 Data

### 192 2.1 Hubble Space Telescope Data

193 Archival observations of Jupiter’s ultraviolet (UV) aurorae made with the Advanced  
194 Camera for Surveys Solar Blind Channel (ACS/SBC) and Space Telescope Imaging Spec-  
195 trograph (STIS) on HST were obtained for this study. These observations comprise more  
196 than 200 cumulative hours of exposure, and span 2007 and 2016–2019; this large sur-  
197 vey is expected to be representative of the general state of Jupiter’s ME aurorae. This  
198 set of observations is available via online archive (Rutala, 2022) with further discussion  
199 and details available in Rutala et al. (2022) and references therein.

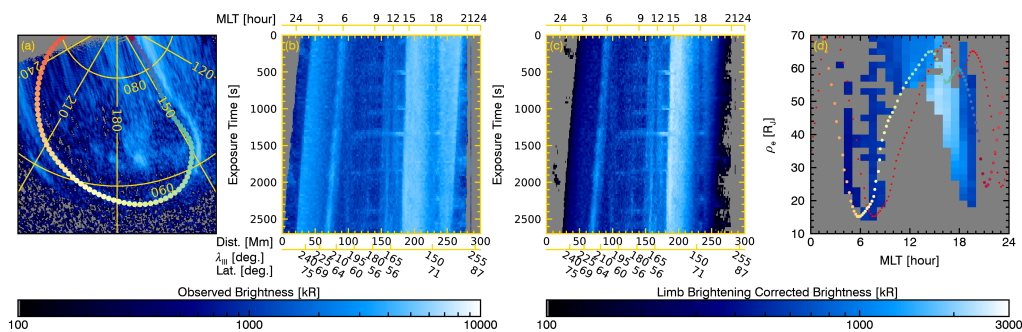


**Figure 1.** Plots showing multiple views of Jupiter’s northern ME on May 22, 2016 beginning at 18:02:46 UTC, as observed with HST STIS. Panel (a) shows a top-down, polar view of the northern ME, with the statistical main oval (SMO) (Nichols et al., 2009) shown (multi-colored points) along with  $\lambda_{III}$  and latitude graticules (yellow lines). Panel (b) shows a labeled keogram, where the observation in (a) is represented in the first (top) row. The values in both (a) and (b) are log-scaled with colors corresponding to the colorbar beneath. Panel (c) depicts the same keogram, but with a limb-brightening correction applied. Panel (d) shows the corrected keogram projected to the magnetospheric equatorial plane as a function of MLT and  $\rho_e$ , with the projected SMO corresponding to the first (multi-colored points, with colors marking the equivalent positions as in panel (a)) and final (red dots) exposures shown. The values in both (c) and (d) are log-scaled, with colors corresponding to the separate colorbar beneath.

Time-tagged STIS observations were split into non-overlapping 30s intervals to create images, while the typical  $\sim 100$ s exposures for the ACS observations were unchanged. Images were reduced and projected onto an equirectangular planetocentric grid using the standard procedures in the Boston University HST data reduction pipeline (e.g. Clarke et al., 2009; Nichols & Cowley, 2022; Rutala et al., 2022); the projection from the HST perspective to an equirectangular grid allows the observations to be viewed from any perspective, as illustrated by the reduced observation mapped to an orthographic polar view in Figure 1a. The factors used to convert the observed auroral brightness from counts/s to kR of unabsorbed H and H<sub>2</sub> emission vary with color ratio (Gustin et al., 2012), which can change rapidly on both small and large scales. Here, we estimate an effective range of color ratio values spanning 5-20 in the ME region from visual inspection of *Juno* ultraviolet spectrograph (UVS)-based maps of the color ratio distribution (G erard et al., 2018, 2020). We adopt a constant color ratio of 12 for converting HST counts/s to kR unabsorbed H<sub>2</sub> emission here; introducing approximate uncertainties in brightness of  $-23\%$  and  $+11\%$  corresponding to the lower and upper bounds of the color ratio range, respectively. These uncertainties are comparable to or smaller than the typical variation in auroral brightness observed in the ME as illustrated in Figure A1, and are not propagated through this analysis as a result. Auroral intensities in the ACS/SBC images were further multiplied by a factor of 1.4 for those using the F115LP filter and 1.6 for those using the F125LP filter, following recent changes to the SBC absolute flux calibration (Avila et al., 2019).

In each reduced image, an ME brightness profile is measured as the mean brightness of the brightest quartile of emission within  $\pm 5^\circ$  perpendicular to the SMO, as found by Nichols et al. (2009), in steps along the ME. 300 steps evenly spaced in distance along the SMO with dynamic sizes were found to maximize resolution while preventing overlap between pixels sampled by adjacent steps. The extracted brightness profile is stacked into a keogram for each image within the same HST visit, and aligned such that the location along the SMO is measured horizontally and exposure time is measured vertically. Figure 1b shows a keogram created in part from the observation in Figure 1a, with SIII coordinates, distance along the SMO, and MLT all labeled. Limb-brightening correction factors found as the inverse cosine of the view angle (Grodent et al., 2005) were applied to each keogram, the results of which are demonstrated in Figure 1c. The inverse-cosine correction assumes a greatly simplified plane-parallel geometry for the aurorae— which in reality have a complex, three-dimensional, time-varying structure— and so generally overestimates the limb-brightening effect very near the edge of planet’s disk as viewed by HST. Nonetheless, the limb-brightening is corrected for as, without it, the dawn sector tends to incorrectly appear as bright as the rest of the ME (Rutala et al., 2022), which is known to not be true statistically (Bonfond et al., 2015) and which would significantly bias the investigation into the variation of the auroral Pedersen conductance with MLT. A more accurate correction factor would be of great use to future auroral studies, particularly those utilizing remote observations. The effect of the overestimation is partially countered by removing all parts of the observations within  $10^\circ$  of the limb; the slight remaining effects of the overestimation will be discussed in the Results. The keogram production process is further discussed in Rutala et al. (2022).

In each of the 288 keograms, the auroral brightness ( $I$ ), local time (LT), latitude ( $\phi$ ), System III longitude ( $\lambda_{III}$ ), and the  $1\sigma$  width ( $\delta\theta$ ) of the ME were recorded for every pixel. Pixels were then mapped from  $\lambda_{III}$  and  $\phi$  in the ionosphere to magnetic local time (MLT) and radial distance in the equatorial plane of the magnetosphere ( $\rho_e$ ) using the magnetic flux equivalence mapping of Vogt et al. (2011). The internal magnetic field for the mapping was specified to be the JRM09 magnetic field model (Connerney et al., 2018) which, over the spatial scales relevant here, is very similar to the more recent JRM33 model (Connerney et al., 2022). Solar CML values for the mapping were found using ephemerides from the NASA NAIF SPICE toolkit (Acton et al., 2018). The angular width of the ME,  $\delta\theta$ , was mapped to a radial width,  $\delta\rho_e$ , in the same manner.

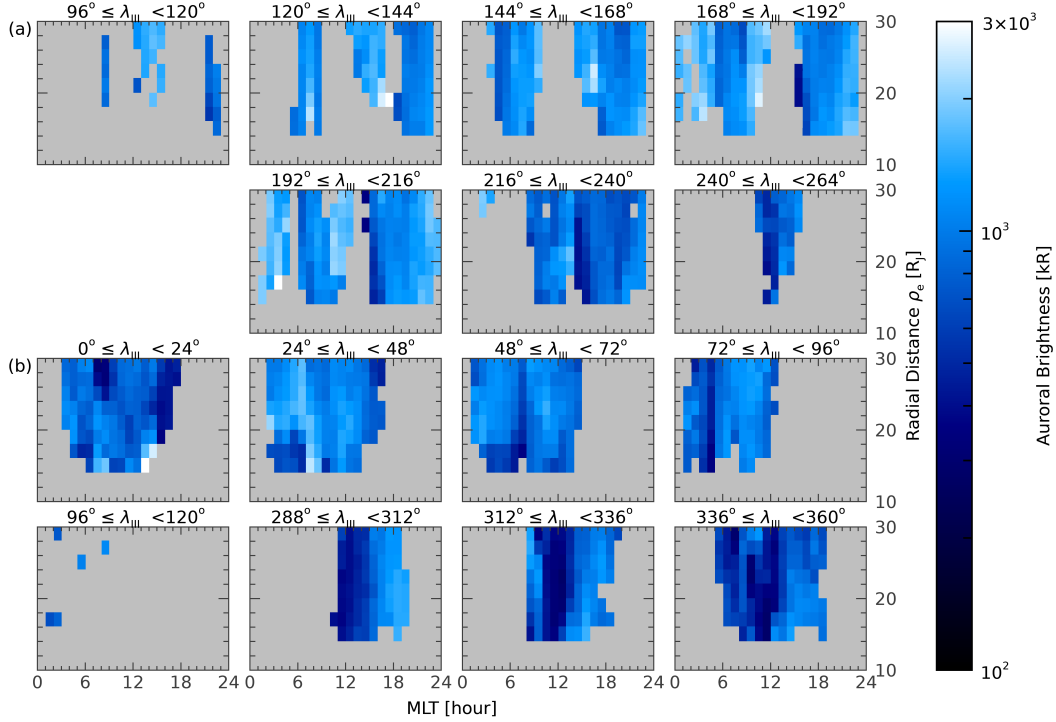


**Figure 2.** Two-dimensional distributions of the auroral brightness for both the (a) northern and (b) southern hemispheres, with colors for each MLT- $\rho_e$  bin corresponding to the colorbar to the right. Each distribution is labeled with the range of solar CMLs it spans; solar CML ranges for which there are no observations were excluded. These distributions show significant structure in MLT,  $\rho_e$ , and solar CML that varies between the northern and southern hemisphere. Auroral emissions near noon in the northern hemisphere occasionally map beyond the 30  $R_J$  limit of these plots, thus leaving no observations in these distributions; where auroral emissions near noon are measured, they tend to be fainter than either dawn or dusk in both hemispheres. Additionally, the northern hemisphere ME aurorae sampled here tend to be brighter than those in the southern hemisphere.

254 The observed and mapped parameters were then binned by 1 hour in MLT, 2  $R_J$  in  $\rho_e$ ,  
 255 and  $24^\circ$  in solar CML; a typical, 40 minute HST observation of the Jovian aurorae spans  
 256  $\sim 24^\circ$  of longitude as the planet rotates. Values in each bin were calculated as the arith-  
 257 metic mean. Figure 1d shows the auroral brightness of the keogram in Figure 1c binned  
 258 in MLT and  $\rho_J$ , with the projected SMO locations corresponding to the first and last  
 259 exposures included for reference. As Figure 1d represents a  $\sim 40$  min. observation, it  
 260 effectively spans a single bin in solar CML and can as such be binned in MLT and  $\rho_e$   
 261 and displayed completely in two dimensions. Emissions mapping to radial distances less  
 262 than that of SMO originate at lower latitudes than the SMO, as is the case particularly  
 263 near dusk in Figure 1. The binned distributions of auroral brightness are shown for the  
 264 full set of observations used here in Figure 2; to display these distributions, which are  
 265 binned in three-dimensional, each panel in Figure 2 represents the two-dimensional dis-  
 266 tribution with respect to MLT and  $\rho_e$  corresponding to a single solar CML bin. While  
 267 the distributions in Figure 1d extend out to 70  $R_J$  to show the full extent of the map-  
 268 ping of the SMO in that configuration, those in Figure 2 only extend to 30  $R_J$  to allow  
 269 direct comparison to the *Galileo*/PLS results discussed in the following section. Context

270 for the distributions in Figure 2, in the form of distributions of both the standard de-  
271 viation and number of observations in each bin, is provided in Figure A1.

## 272 2.2 *Galileo* PLS Measurements

273 Plasma parameters used here are derived exclusively from the numerical moments  
274 of *Galileo*/PLS real-time science data as provided by Frank et al. (2023). While the ad-  
275 dition of more recent plasma data from the *Juno*/JADE plasma experiment would prove  
276 useful in this analysis, the numerical moments, including velocity, for these ion data are  
277 not yet publicly available, nor have the experiment’s data been cross-calibrated for di-  
278 rect comparison to *Galileo*/PLS data. Both of these analyses would be significant con-  
279 tributions to understanding the Jovian magnetospheric plasma population, but are be-  
280 yond the scope of the present study. The *Galileo* spacecraft’s native Inertial Rotor Co-  
281 ordinate (IRC) system, a despun coordinate system based on the spacecraft’s geometry,  
282 is complex (Bagenal et al., 2016) and has not been fully implemented into SPICE (Acton  
283 et al., 2018), due in part to the *Galileo* spacecraft heritage predating the SPICE toolkit.  
284 SPICE ephemerides for the *Galileo* spacecraft position are available for all 6751 moments;  
285 spacecraft pointing information is only available for 4897 of those 6751. So that the full  
286 set of moments can be used, the plasma flow speed is estimated as the root-sum-square  
287 of all the velocity components, as the azimuthal component of the plasma velocity is ex-  
288 pected to be much larger than the radial and polar components.

289 These numerical moments span 31 of *Galileo*’s 34 orbits, and cover a combined 129  
290 days. The plasma parameters span  $10R_J \leq \rho_e \leq 30R_J$  within  $\sim 1 - 2R_J$  of the equa-  
291 torial plane, with larger distances from the equatorial plane corresponding to larger ra-  
292 dial distances. These parameters cover all local times and SIII longitudes, with a bias  
293 in local time sampling towards dawn and dusk. Figure 3 illustrates the coverage of the  
294 numerical moments relative to *Galileo*’s full orbit and shows this bias. Figures 3a and  
295 3b are plotted in the Jupiter-De-Spun-Sun (JSS) reference frame, which is defined to have

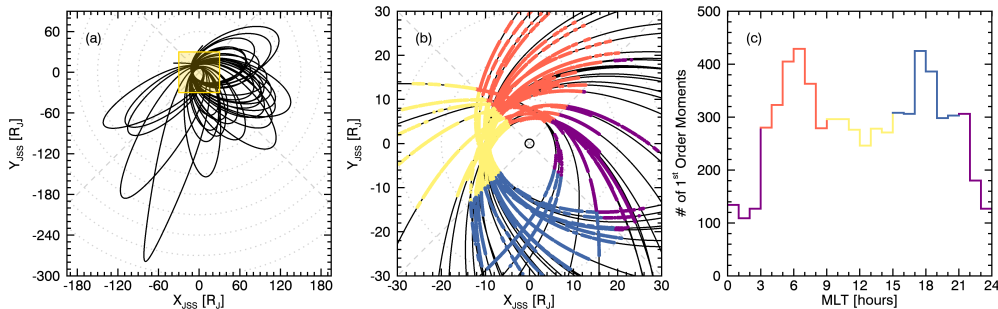


**Figure 3.** Plots illustrating *Galileo* PLS coverage of the magnetosphere. Plot (a) shows all 34 *Galileo* orbits projected into Jupiter’s equatorial plane in the Jupiter-Despun-Sun (JSS) reference frame, with the region spanning  $\pm 30R_J$  in both dimensions highlighted in yellow. (b) A zoomed-in view of the highlighted region in (a), with individual *Galileo* PLS plasma flow speed measurements overplotted as points, colored according to MLT sector: dawn ( $03 \leq \text{MLT} < 09$ ) in orange, noon ( $09 \leq \text{MLT} < 15$ ) in yellow, dusk ( $15 \leq \text{MLT} < 21$ ) in blue, and mid-night ( $00 \leq \text{MLT} < 03$ ;  $21 \leq \text{MLT} < 24$ ) in purple. (c) A histogram of the number of *Galileo* PLS plasma flow speed measurements in each hour-wide MLT bin. The abundance of dawn and dusk observations, compared to those near noon and particularly near midnight, is evident.

296  $\hat{Z}$  aligned with Jupiter’s rotational axis, the Sun located in the  $\hat{X}-\hat{Z}$  plane, and  $\hat{Y}$  com-  
 297 pleting the right-hand orthogonal set. The average plasma corotation rate ( $R_C$ ) was cal-  
 298 culated for bins spanning 1 hour in MLT and 2  $R_J$  in  $\rho_e$ ; as the middle magnetosphere  
 299 is dominated by magnetic local time effects rather than longitudinal effects (Vogt et al.,  
 300 2011; Ray et al., 2014), the *Galileo* data were not binned by the solar CML of the planet.  
 301 Binning of the plasma parameters was performed by averaging with weights proportional  
 302 to the inverse of the parameter variance to be representative of the time-averaged MI-  
 303 coupled system.

304 The plasma corotation rate  $R_C$  is defined as

$$305 \quad R_C = \frac{v_{flow}}{\rho_e \Omega_J} = \frac{\omega_{flow}}{\Omega_J} \quad (1)$$

306 where  $v_{flow}$  is the calculated linear plasma flow velocity from the *Galileo* PLS data,  $\omega_{flow}$   
 307 is the angular plasma flow velocity ( $\omega_{flow} = v_{flow}/\rho_e$ ), and  $\Omega_J$  is the angular veloc-  
 308 ity at which Jupiter rotates ( $1.76 \times 10^{-4}$  rad  $s^{-1}$ ).  $R_C$  is averaged in each bin rather  
 309 than  $v_{flow}$  to account for the expected inverse relationship between equatorial distance  
 310  $\rho_e$  and  $v_{flow}$ . When  $v_{flow} = \rho_e \Omega_J$ , the plasma is rigidly corotating with the planet and  
 311  $R_C = 1$ . In turn, when  $v_{flow} = 0$  then the plasma is fixed with respect to the Sun-  
 312 Jupiter geometry, or effectively fixed in MLT, and  $R_C = 0$ . The full set of 6751 plasma  
 313 parameters used from *Galileo* PLS are summarized in Figure 4, which shows the two-  
 314 dimensional distributions of the corotation rate  $R_C$  with respect to MLT and  $\rho_e$ . The  
 315 distributions of the standard deviations and number of measurements in each bin are pro-  
 316 vided in Figure A2 for context in interpreting Figure 4.

### 317 3 Analysis

318 The field-aligned current per radian of azimuth,  $I_{||}$ , flowing near the ionosphere in  
 319 the coupled MI system responsible for accelerating electrons into Jupiter’s ionosphere  
 320 and driving the planet’s ME can be found as

$$I_{||} = -2 \int_0^{\rho_e} j_z \rho'_e d\rho'_e \quad (2a)$$

$$= 4 \Sigma_P^* \Omega_J (1 - R_C) F_e \quad (2b)$$

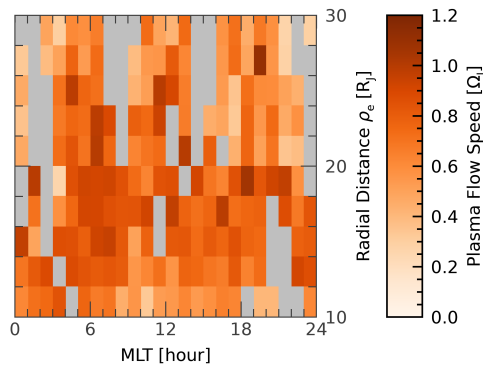


**Figure 4.** Two-dimensional distribution of the corotation rate  $R_C$  of the equatorial plasma from *Galileo* PLS moments from Equation 1. The moments were not binned with respect to solar CML, as the middle magnetosphere is expected to vary primarily in MLT. It is difficult to make out clear patterns in  $R_C$ , except that there is a slight tendency for higher values near dawn than near dusk.

321 adapted from Equation 16 in Cowley and Bunce (2001). Here  $j_z$  is the field-aligned cur-  
 322 rent density flowing out of the current sheet lying in the middle magnetosphere's equa-  
 323 torial region,  $\Sigma_P^*$  is the height-integrated effective Pedersen conductance,  $\Omega_J$  and  $R_C$   
 324 are as previously defined, and  $F_e$  is the equatorial magnetic flux function, a function which  
 325 maps the auroral ionosphere to the equatorial middle magnetosphere along contours of  
 326 constant magnetic flux. The field-aligned current per radian of azimuth  $I_{||}$  can be cal-  
 327 culated from the auroral brightness observed with HST using Equation 2a and from the  
 328 plasma flow speed derived from *Galileo* PLS using Equation 2b, as will be discussed in  
 329 Sections 3.1 and 3.2, respectively.

### 330 3.1 Field-aligned currents from HST observations

331 The brightness of the ME aurorae observed with HST is directly proportional to  
 332 the precipitated energy flux of auroral electrons  $E_f$  incident on the atmosphere, with a  
 333 typical conversion factor of 10 kR per 1 mW m<sup>-2</sup>. This conversion factor is an average  
 334 of multiple studies (Gerard & Singh, 1982; Waite Jr. et al., 1983; Grodent et al., 2001;  
 335 Gustin et al., 2012; Nichols & Cowley, 2022) which is expected to be valid for the range  
 336 of precipitating electron energies (0.5 – 150 keV) (Gustin et al., 2012) expected to re-  
 337 sult from the field-aligned currents (Knight, 1973). This energy flux  $E_f$  is in turn related  
 338 to the field-aligned current density just above the auroral ionosphere  $j_{||}$  as

$$j_{||} = j_{||,0} \left( \pm \sqrt{2 \frac{E_f}{E_{f,0}} - 1} \right) \quad (3)$$

339 where  $j_{||,0}$  is the maximum field-aligned current density above the ionosphere and  $E_{f,0}$   
 340 is the maximum precipitated energy flux of auroral electrons, both for the case of an ab-  
 341 sence of field-aligned potentials. Equation 3 is derived by assuming the minimum nec-  
 342 essary field-aligned potentials for currents to flow into the ionosphere. The maximum  
 343 energy flux in the absence of field-aligned potentials is  $E_{f,0} = 2N\sqrt{W_{th}/2\pi m_e}W_{th}$  (Equa-  
 344 tion 37 in Cowley and Bunce (2001)), which is a number flux of electrons ( $2N\sqrt{W_{th}/2\pi m_e}$ )  
 345 multiplied by a characteristic energy ( $W_{th}$ ).  $E_{f,0}$  can therefore be estimated by measur-  
 346 able physical parameters; here,  $N = 0.018 \text{ cm}^{-3}$  (Bagenal et al., 2016; Huscher et al.,  
 347 2021) and  $W_{th} = 5 \text{ keV}$  (Allegrini et al., 2021) are used. Similarly, the maximum field-  
 348 aligned current density just above the ionosphere in the absence of field-aligned poten-  
 349 tials is  $j_{||,0} = eN\sqrt{W_{th}/2\pi m_e}$ , the number flux of electrons multiplied by  $e$ , the ele-  
 350 mentary charge (Equation 28 in Cowley and Bunce (2001)).

351 The quantity  $j/B$  is constant along a magnetic field line provided there are no field-  
 352 perpendicular currents intersecting the field line outside of the equatorial and ionospheric  
 353 regions (Cowley & Bunce, 2001), so  $j_{||}$  can be written as  $j_z B_i / B_e$ , where  $B_i$  and  $B_e$   
 354 are the strengths of the magnetic field along the field line in the ionosphere and the current  
 355 sheet in the equatorial plane, respectively. The magnetic field strength in the equato-  
 356 rial plane of the magnetosphere  $B_e$ , is calculated from the form provided in Vogt et al.  
 357 (2011), which is itself a fit to in-situ magnetic field measurements from *Pioneer 10*, *Pi-*  
 358 *oneer 11*, *Voyager 1*, *Voyager 2*, *Ulysses*, and *Galileo* spanning 20–120 R<sub>J</sub>. The mag-  
 359 netic field strength in the ionosphere was found using the internal magnetic field model  
 360 based on *Juno*'s first 33 orbits of Connerney et al. (2022)(henceforth, JRM33), calcu-  
 361 lated to order 13 using the code provided by Wilson et al. (2023), and assuming an al-  
 362 titude of 1R<sub>J</sub>. Vogt et al. (2011) The JRM33 internal field model is inappropriate for  
 363 use in the middle and outer magnetosphere, as the higher-order terms become negligi-  
 364 ble and the resulting modeled field becomes unphysically azimuthally symmetric. The  
 365 form of the equatorial magnetic field  $B_e$  is adopted instead from Vogt et al. (2011) rather  
 366 than the Connerney et al. (2020) magnetodisk model to allow for the middle and outer  
 367 magnetosphere to vary with MLT.

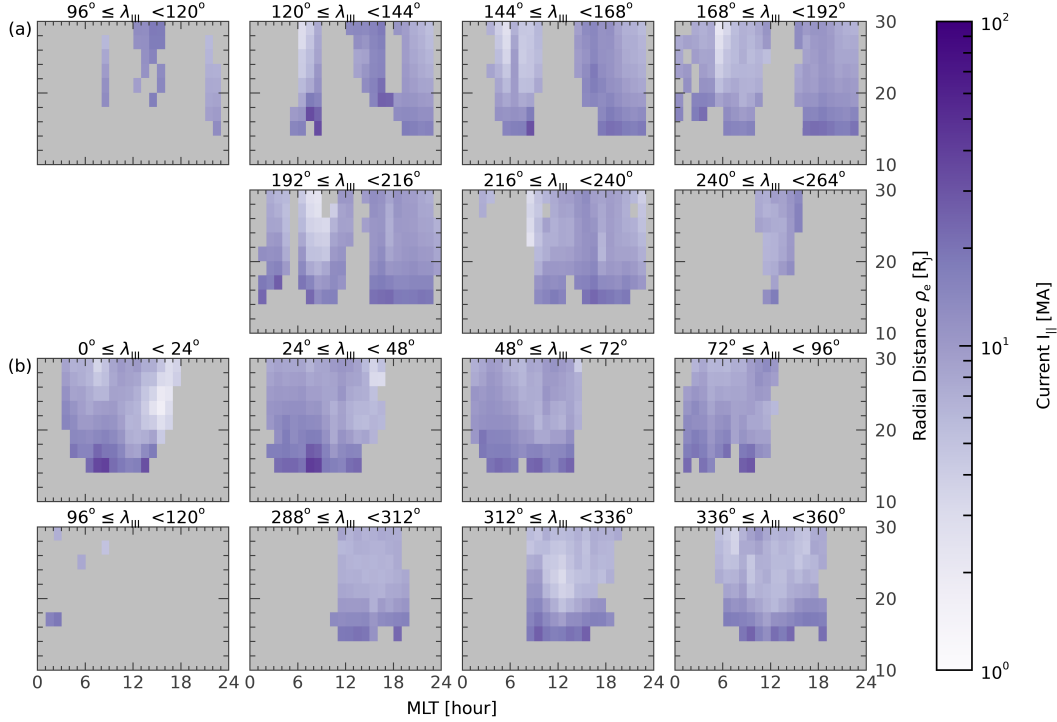


**Figure 5.** Two-dimensional distributions of the integrated field-aligned current per radian of azimuth  $I_{||}$  calculated from Equation 4 for the (a) northern and (b) southern hemispheres, with colors for each MLT- $\rho_e$  bin corresponding to the colorbars to the right. Each distribution is labeled with the range of solar CMLs it covers; solar CML bins with no coverage are excluded. The hemispheric asymmetry seen clearly in Figure 2 is no longer evident after converting to field-aligned current. There is a general trend towards higher currents when the magnetosphere is more perturbed (i.e., when the ME maps to closer in regions of the magnetosphere) and a slight trend towards stronger currents near dusk than near dawn.

368

Equation 3 can thus be substituted into Equation 2a for  $j_z$  to give

$$I_{||} = -2 \int_0^{\rho_e} j_{||,0} \frac{B_e}{B_i} \left( \pm \sqrt{2 \frac{E_f}{E_{f,0}} - 1} \right) \rho'_e d\rho'_e \quad (4)$$

369

370

371

372

373

374

375

376

377

378

379

380

381

382

383

which can be used to calculate the field-aligned current per radian of azimuth  $I_{||}$  corresponding to a given auroral brightness. Evaluation of Equation 4 requires an integrable auroral electron energy flux  $E_f(\rho'_e)$ , which in turn requires a function of the auroral brightness over equatorial distance. The variation of the auroral brightness with equatorial distance illustrated in Figure 2 does not represent this function directly. Instead, these distributions show the typical values of the observed ME when the ME maps to a given location in MLT- $\rho_e$  space, which in turn represents the maximum of the field-aligned current density  $j_z$  for a given span of solar CML. An integrable radial distribution of  $E_f(\rho'_e)$  is therefore approximated as a Gaussian having a peak value of  $E_f$ , a center defined by the corresponding radial bin, and a width defined by the angular width of the ME ( $\delta\theta$ ) magnetospherically mapped to a radial width ( $\delta\rho_e$ ). The resulting radial distributions are then numerically integrated from 0 out to the corresponding  $\rho_e$  value. The resulting values of  $I_{||}$  we report are thus average field-aligned currents per radian of azimuth entering the ionosphere at the ME when the location of the ME maps to the current sheet at the location specified by the corresponding bin. The distributions of  $I_{||}$  with MLT,

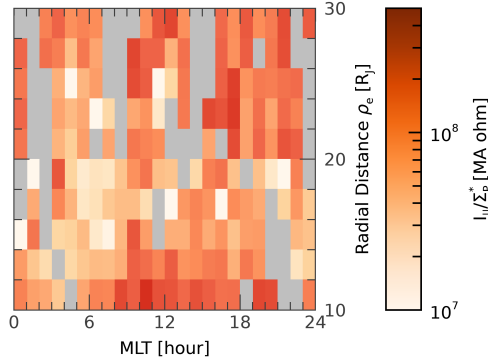


**Figure 6.** Two-dimensional distribution of the quantity  $I_{||}/\Sigma_P^*$  derived from the *Galileo* PLS moments using Equation 5, with colors in each MLT- $\rho_e$  bin corresponding to the colorbar to the right. While the parameter  $I_{||}/\Sigma_P^*$  is not strongly structured in either MLT or equatorial distance  $\rho_e$ , it can be seen to generally be smaller at dawn than at dusk, inverting the pattern seen in Figure 4.

384  $\rho_e$ , and solar CML in Figure 5 thus illustrate various independent MI coupling configurations rather than multiple samples of the same configuration; similarly, the distributions of the standard deviation of  $I_{||}$  presented in Figure A3 represent the variability of each of these configurations, rather than a level of confidence which varies with distance  $\rho_e$ . To clarify further, the distributions of  $I_{||}$  calculated here are not expected to increase monotonically with equatorial distance  $\rho_e$ , even though the integral of  $F_e(\rho_e')$  would, for the same reasons that the ME brightness does not increase monotonically with  $\rho_e$  in Figure 2.

### 392 3.2 Field-aligned currents from Galileo-PLS data

393 Returning to Equation 2b and rearranging, the total field-aligned current per radian of azimuth  $I_{||}$  flowing into the ionosphere divided by the effective, height-integrated Pedersen conductance  $\Sigma_P^*$  of the ionosphere, can be found as

$$\frac{I_{||}}{\Sigma_P^*} = 4\Omega_J(1 - R_c)F_e \quad (5)$$

396 The height-integrated effective Pedersen conductance  $\Sigma_P^*$  is the sum of all conductance terms and is reduced from the true value,  $\Sigma_P$ , by a factor of  $(1-k)$  to account for the slippage in the ion-neutral coupling in the ionosphere. The values of  $k$  range from  $0 < k < 1$ , with  $k = 0$  corresponding to no slippage of the neutral atmosphere relative to the planet's rigid rotation rate and  $k \approx 1$  corresponding to maximal slippage (Huang & Hill, 1989; Nichols & Cowley, 2003). The equatorial flux  $F_e$ , which relates locations in the ionosphere to conjugate points in the current sheet in the equatorial plane of the magnetosphere along contours of constant magnetic flux, is a function of both MLT and  $\rho_e$  and is calculated using the form provided by Ray et al. (2014). This description of  $F_e(\text{MLT}, \rho_e)$  is based on a slightly modified version of the empirical magnetic field model used to map HST observations into the equatorial magnetospheric plane (Vogt et al., 2011). The differences between this and the unmodified empirical magnetic field model are greatest near the planet; the two descriptions agree throughout the middle magnetosphere where MI coupling currents flow, ensuring consistency between the values derived from *Galileo* PLS and HST observations.

411 The quantity  $I_{\parallel}/\Sigma_P^*$  can thus be solved for using *Galileo* PLS-derived values of the  
 412 plasma corotation rate  $R_c$  and the known form of  $F_e$ . This quantity is introduced for  
 413 convenience and has limited physical meaning, despite having the form of an electric po-  
 414 tential. Instead, the quantity  $I_{\parallel}/\Sigma_P^*$  groups unknown parameters together, and will al-  
 415 low further exploration of the distribution of  $\Sigma_P^*$  when compared to the values of  $I_{\parallel}$  de-  
 416 rived from HST observations. Figure 6 shows the distributions of the quantity  $I_{\parallel}/\Sigma_P^*$   
 417 with MLT and equatorial distance  $\rho_e$ , while the standard deviations of each bin are in-  
 418 cluded in Figure A4 for context.

## 419 4 Results and Discussion

### 420 4.1 Azimuthally integrated field-aligned currents

421 First, we focus on the field-aligned current per radian azimuth  $I_{\parallel}$  derived from HST  
 422 observations, which, unlike the parameter  $I_{\parallel}/\Sigma_P^*$  derived from *Galileo* measurements,  
 423 is representative of the field-aligned auroral currents flowing in Jupiter’s coupled MI sys-  
 424 tem without any further assumptions about the ionospheric Pedersen conductance. The  
 425 northern ME is found to have a median current per radian of azimuth of  $I_{\parallel} = 9.34^{+5.72}_{-3.54}$   
 426 MA rad<sup>-1</sup>, while the southern ME has a median current per radian of azimuth of  $I_{\parallel} =$   
 427  $8.61^{+6.77}_{-3.05}$  MA rad<sup>-1</sup>. These median values are found using a Monte Carlo bootstrap anal-  
 428 ysis with lognormal error perturbation (henceforth just “medians”), in order to better  
 429 account for the measurement errors in the non-Gaussian distribution of currents (Curran,  
 430 2014). Upper and lower errors correspond to the 84<sup>th</sup> and 16<sup>th</sup> percentiles, respectively,  
 431 to approximate  $1\sigma$  errors.

432 These median currents are in very good agreement with the currents calculated from  
 433 *Juno* magnetometer measurements. In the northern hemisphere, the median field-aligned  
 434 current compares favorably with the values of  $\sim 3.8$  MA rad<sup>-1</sup> (within  $\sim 1.6\sigma$ ) and  $\sim 5.4$   
 435 MA rad<sup>-1</sup> (within  $\sim 1.1\sigma$ ) and, considering that 95% of the currents calculated here have  
 436 values between  $2.82 < I_{\parallel} < 24.3$  MA rad<sup>-1</sup>, aligns very well with the measured range  
 437 of  $\sim 1 - 27$  MA rad<sup>-1</sup> (Kotsiaros et al., 2019; Kamran et al., 2022; Nichols & Cowley,  
 438 2022, respectively). In the southern hemisphere, the median field aligned current agrees  
 439 more strongly with the value of  $\sim 9.2$  MA rad<sup>-1</sup> (within  $\sim 0.09\sigma$ ) and lies well within the  
 440 same  $\sim 1 - 27$  MA rad<sup>-1</sup> range as 95% of the calculated currents have values in the range  
 441  $2.94 < I_{\parallel} < 25.8$  MA rad<sup>-1</sup> (Kotsiaros et al., 2019; Nichols & Cowley, 2022, respec-  
 442 tively). Each median current derived here is also in good agreement with hemisphere-  
 443 symmetric MI coupling theory values of  $\sim 7.1$  MA rad<sup>-1</sup> (within  $\sim 0.5\sigma$  and  $\sim 0.6\sigma$  for  
 444 the northern and southern hemispheres respectively) (Cowley et al., 2008). The hemi-  
 445 spheric asymmetry found from analysis of low-altitude *Juno*/MAG data (Kotsiaros et  
 446 al., 2019) is not recovered in the medians reported here, but some sense of this asymme-  
 447 try is recovered by this analysis in that the reported 84<sup>th</sup> percentile value of the south-  
 448 ern median current is larger than that of the northern median current. Considering the  
 449 full two-dimensional distributions of the median currents  $I_{\parallel}$  found here, Figure 5 shows  
 450 that there is a slight tendency toward larger field-aligned currents near dusk rather than  
 451 near dawn, with occasional weak currents present near noon. This is qualitatively sim-  
 452 ilar to the distribution of field-aligned current densities found from the magnetic field  
 453 signatures of lobe traversals within 30 R<sub>J</sub>, and thus validates the importance of azimuthal  
 454 magnetodisk currents in determining the locations of field-aligned currents (Lorch et al.,  
 455 2020).

### 456 4.2 Effective Pedersen conductance

457 The effective Pedersen conductance ( $\Sigma_P^*$ ) can be calculated by dividing the field-  
 458 aligned current per radian of azimuth derived from HST measurements  $I_{\parallel}$  by the quan-  
 459 tity derived from *Galileo* PLS moments  $I_{\parallel}/\Sigma_P^*$ . Figure 7 shows distributions of this cal-  
 460 culated effective Pedersen conductance for the northern and southern hemispheres; the

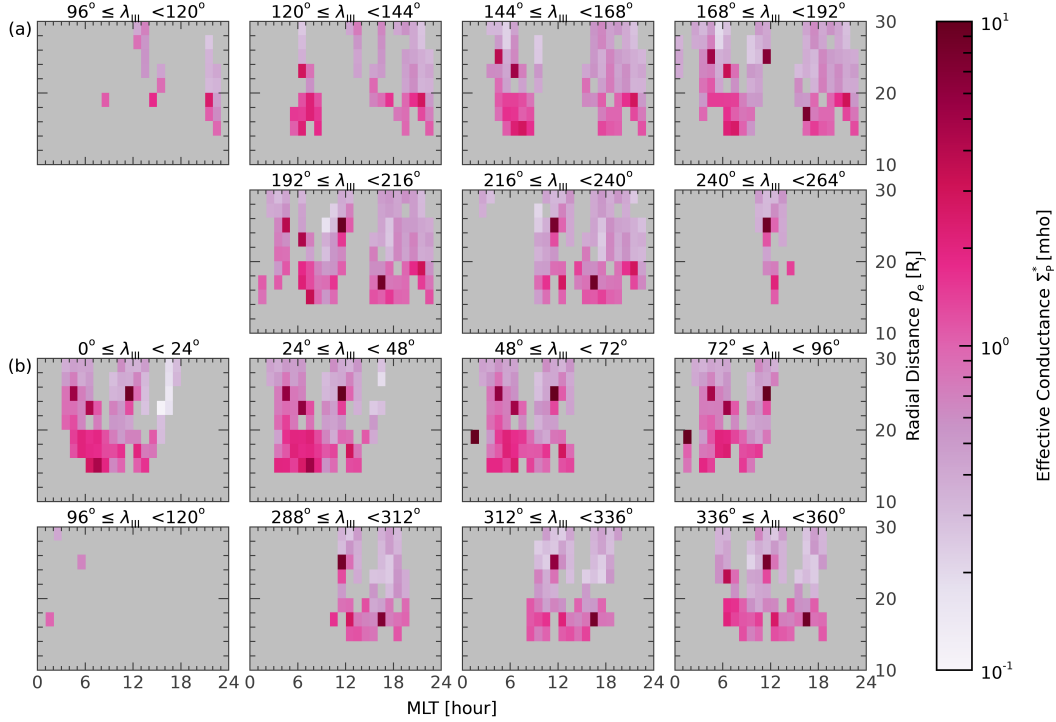


**Figure 7.** Two-dimensional distributions of the effective Pedersen conductance  $\Sigma_P^*$  for the (a) northern and (b) southern hemispheres, with the color of each MLT- $\rho_e$  bin corresponding to the colorbars to the right. Each distribution is labeled with the range of solar CMLs it covers. The effective Pedersen conductance is only calculated where both HST-derived and *Galileo*/PLS-derived data are present; solar CML bins with no coverage are excluded. The conductance is generally greatest at smaller radial distances, as might be expected during a magnetospheric compression event where strong field-aligned currents are driven atypically close to the planet.

461 distributions of the standard deviation of the effective Pedersen conductance are shown  
 462 in Figure A5 in order to provide a full picture of the variation. The binned distributions  
 463 of  $I_{\parallel}/\Sigma_P^*$  are assumed to be the same at all solar CML in this analysis. We find 95% of  
 464 conductances lie in the range  $0.03 < \Sigma_P^* < 1.66$  mho in the north with a median of  $\Sigma_P^* =$   
 465  $0.13_{-0.07}^{+0.26}$  mho and  $0.03 < \Sigma_P^* < 2.40$  mho in the south with a median of  $\Sigma_P^* = 0.16_{-0.10}^{+0.34}$   
 466 mho, with errors corresponding to the 16<sup>th</sup> and 84<sup>th</sup> percentiles.

467 For an average value of  $k = 0.55$ , well within typical values of  $k \approx 0.4-0.7$  (Millward  
 468 et al., 2005), the values of the true Pedersen conductance we find are  $\Sigma_P = 0.3_{-0.2}^{+0.6}$  mho  
 469 with 95% having values between  $0.07 \sim 4$  mho in the northern hemisphere and  $\Sigma_P = 0.4_{-0.2}^{+0.8}$   
 470 mho with 95% having values between  $0.07 \sim 5$  mho in the southern hemisphere, where  
 471 we have rounded due to the large uncertainties in the value of  $k$ ; for  $k = 0.7$ , the median  
 472 Pedersen conductances are as high as  $\Sigma_P = 0.4_{-0.2}^{+0.9}$  mho in the north and  $\Sigma_P =$   
 473  $0.5_{-0.3}^{+1.1}$  in the south. These averages are comparable to theoretical estimates (Millward  
 474 et al., 2002, 2005) but generally lower than recent estimates made using *Juno* ultraviolet  
 475 spectrograph (UVS) measurements and ionospheric modeling (Wang et al., 2021;  
 476 Al Saati et al., 2022) of  $\Sigma_P \approx 2$  (within  $\sim 3.0\sigma$  for  $k = 0.55$  and  $\sim 1.8\sigma$  for  $k = 0.7$ )  
 477 in the northern hemisphere and  $\Sigma_P \approx 3$  (within  $\sim 3.5\sigma$  for  $k = 0.55$  and  $\sim 2.2\sigma$  for  $k =$   
 478  $0.7$ ) in the southern hemisphere. While some of this discrepancy may be attributed to  
 479 the uncertainty in  $k$  value, a more significant source likely lies in differences in methods

480 between studies. The mean values of  $\Sigma_P$  given by Al Saati et al. (2022) are calculated  
481 using only peak values, while those reported here are averaged over the top quartile of  
482 all values (Rutala et al., 2022). Visual inspection of maps of the Pedersen conductance  
483 based on *Juno*/UVS data and ionospheric modeling suggests a somewhat lower typical  
484 Pedersen conductance of  $\Sigma_P \approx 1$  mho (within  $\sim 1.2\sigma$  ( $k = 0.55$ ) or  $\sim 0.7\sigma$  ( $k = 0.7$ )  
485 in the north and  $\sim 0.9\sigma$  ( $k = 0.55$ ) or  $\sim 0.4\sigma$  ( $k = 0.7$ ) in the south) when averaged  
486 over a wider range immediately surrounding the ME. A general north-south symmetry  
487 in the mean Pedersen conductance is common to our results, theoretical models (Millward  
488 et al., 2002, 2005), and *Juno*/UVS-based findings (Gérard et al., 2020, 2021; Wang et  
489 al., 2021; Al Saati et al., 2022).

490 For clarity, Figure 8 shows the same data as Figure 7, but with the medians and  
491 the 84<sup>th</sup>/16<sup>th</sup> percentile errors of the effective Pedersen conductance in each bin plot-  
492 ted. By comparison to the average values and errors for each hemisphere overall, the vari-  
493 ations in conductance with respect to each binning parameter can be seen. Figures 8c  
494 and 8f show that  $\Sigma_P^*$  varies minimally with solar CML. Figures 8b and 8e show that the  
495 effective Pedersen conductance is generally higher at smaller radial values, correspond-  
496 ing to higher field-aligned currents when the magnetosphere is in a disturbed enough state  
497 for the ME to map to these distances. The conductance thus increases with current, as  
498 expected (Nichols & Cowley, 2004). The bin-to-bin variation is greatest when the con-  
499 ductance is interpreted as a function of MLT, as shown in Figures 8a and 8d. This sig-  
500 nificant variation in effective conductance with MLT is more likely than the variations  
501 with equatorial distance or solar CML to be related to the local time asymmetries in the  
502 appearance, distribution, and motion of ME aurorae. Both hemispheres display peaks  
503 in the effective conductance between 6–9, 12–13, and 14–15 MLT. It is worth not-  
504 ing that, without the limb-brightening correction applied to HST-observed auroral bright-  
505 ness, derived field-aligned currents would be increased more near dawn and dusk than  
506 near noon, and  $\Sigma_P^*$  would increase proportionally. The overestimation of the limb-brightening  
507 correction factors thus results in an underestimation of the conductance near the planet’s  
508 limbs at dawn and dusk, and a more accurate model of Jupiter’s limb-brightening would  
509 heighten the peak in  $\Sigma_P^*$  between 6–9 MLT further than the others.

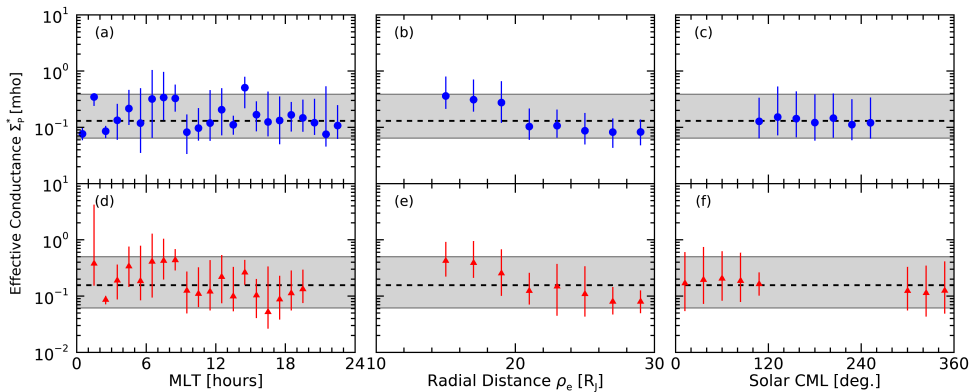


**Figure 8.** Plots more clearly showing the trends in the median effective Pedersen conduc-  
tance  $\Sigma_P^*$  with MLT (a, d),  $\rho_e$  (b, e), and solar CML (c, f) for the northern (a, b, c; blue circles)  
and southern (d, e, f; red triangles) hemisphere ME. The overall median effective Pedersen con-  
ductance (dashed line) along with the 84<sup>th</sup> and 16<sup>th</sup> percentile errors (gray shaded region) on  
this value are shown for context. The conductance is generally higher near dawn than elsewhere  
within the ME, and higher at smaller radial distances as seen in Figure 7. In contrast, the con-  
ductance varies insignificantly with solar CML.

510 Figure 9 shows the complete conductance distributions mapped onto Jupiter’s au-  
 511 roral ionosphere for each solar CML bin, allowing the variation in  $\Sigma_P^*$  with local time  
 512 and location relative to the SMO to be visualized. The generally increased effective Ped-  
 513 ersen conductance near local dawn, located to the left of each frame in Figure 9, is ev-  
 514 ident. The smooth decrease in  $\Sigma_P^*$  with increasing  $\rho_e$  can be seen as a decrease in  $\Sigma_P^*$   
 515 with increasing latitude, particularly in the noon and dusk sectors, in Figure 9a. The  
 516 same trend is not seen in Figure 9b, as the middle magnetosphere maps to a smaller range  
 517 of latitudes in the southern ME than in the northern ME.

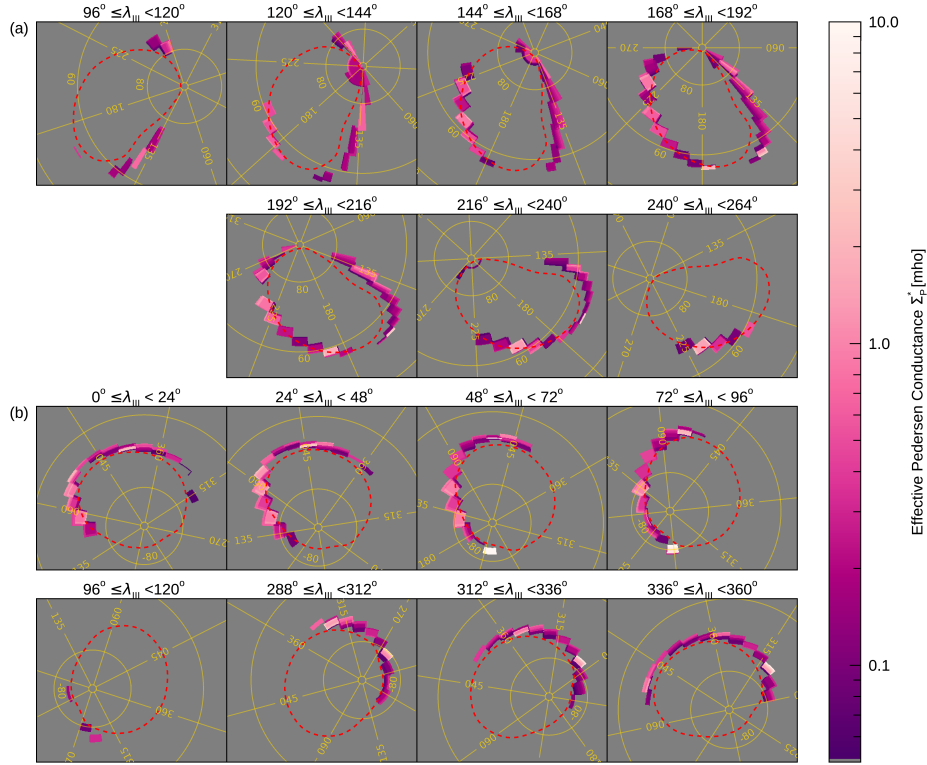


**Figure 9.** Polar, orthographic views of Jupiter’s northern (a) and southern (b) auroral re-  
 gions, with the derived  $\Sigma_P^*$  distributions shown mapped onto the planet by mapping MLT and  $\rho_e$   
 onto  $\lambda_{III}$  and  $\phi$ . Each frame corresponds to one solar CML bin as labeled above with the mean  
 solar CML, and hence noon local time, located at the bottom of the frame in the northern hemi-  
 sphere (a) and at the top of the frame in the southern hemisphere (b); solar CML bins with no  
 coverage are excluded. The SMO (red dashed line) (Nichols et al., 2009) and  $\lambda_{III}$  and  $\phi$  gratic-  
 ules (yellow lines) are shown. Values of  $\Sigma_P^*$  have been log-scaled and correspond to the colorbar  
 to the right. The increased conductance near dawn (left of each frame) can be seen, as can the  
 increased conductance at lower latitudes (mapping to smaller  $\rho_e$ ).

518 From the derived distributions of  $\Sigma_P^*$  alone, we cannot determine the cause of the  
 519 variation of the conductance with MLT. It is of interest, however, that the effective Ped-  
 520 ersen conductance peaks in the late-dawn (6 – 9 MLT) and noon (12 – 13 MLT) re-  
 521 gions are generally collocated with known subcorotating emission features within the ME:  
 522 the dawn storms and associated, less bright subcorotating emission features in the post-  
 523 dawn region (Rutala et al., 2022) and the noon discontinuity and auroral spot near noon  
 524 (Radioti et al., 2008; Palmaerts et al., 2014).

525 The co-occurrence of increased ionospheric conductance and subcorotating auro-  
 526 ral features within the ME was hypothesized by Rutala et al. (2022) as an explanation  
 527 of subcorotational behavior near dawn. The basic premise being that, if the ionospheric  
 528 conductance is locally increased for a reason unrelated to MI-coupling currents, the MI-  
 529 coupling currents will increase in magnitude due to the heightened conductance, accel-  
 530 erating magnetospheric plasma up to the corotation rate of the planet; as the magne-  
 531 tosphere generally compresses from dawn through noon, the linear velocity of the recently-  
 532 accelerated magnetospheric plasma would exceed the local angular corotational veloc-  
 533 ity as the system rotates, thus reducing or reversing the field-aligned currents. In the iono-  
 534 sphere, this would appear as a bright auroral form associated with the increased currents  
 535 which ends abruptly as the currents reverse, thus appearing fixed in local time. This pic-  
 536 ture meshes well with the noon ME discontinuity observed by Radioti et al. (2008), which  
 537 is expected to be associated with reduced or reversed field-aligned currents. The secondary  
 538 peak in  $\Sigma_P^*$  near noon may be associated with the subcorotational noon auroral spot (Palmaerts  
 539 et al., 2014), as following noon the magnetosphere expands again, thus requiring increased  
 540 field-aligned currents to bring plasma up to local corotational velocity.

541 This second peak in  $\Sigma_P^*$  near 12 MLT may instead be caused by increased field-  
 542 aligned currents caused by shearing motions of magnetospheric plasma, as modeled by  
 543 Chané et al. (2018). Generally, as an increase in the field-aligned currents will cause an  
 544 increase in the effective Pedersen conductance, we cannot distinguish between cause and  
 545 effect with this data set: high currents could cause increased conductance, or heightened  
 546 conductance may drive increased currents. It is of note that the conductance distribu-  
 547 tions found in Figure 8 are more similar to the modeled conductance distribution in LT  
 548 found by Tao et al. (2010) than to the distributions in solar CML found by Gérard et  
 549 al. (2020, 2021) from ionospheric modeling based on *Juno*/UVS data. In the latter case,  
 550 the differences may in part be explained by the difference in observational integration  
 551 time. Images from HST span non-overlapping 30–100 s exposures while spectral im-  
 552 ages from *Juno*/UVS were integrated over 20–50 min (Gérard et al., 2020, 2021), which  
 553 would introduce more smoothing into the *Juno* UVS based maps than is present in this  
 554 analysis. Further, the differences in methodology between the spatial analysis of Gérard  
 555 et al. (2020), which is a case study of 8 individual *Juno* orbits, and the long-term sta-  
 556 tistical study presented here may contribute significantly to the apparent differences be-  
 557 tween the two. A careful comparison between *Juno*/UVS-derived conductance and con-  
 558 temporary *Juno*/JADE-derived plasma flow, similar to the analysis performed here, is  
 559 needed to fully explore these potential differences. Conversely, the similarity in form be-  
 560 tween the  $\Sigma_P^*$  distributions found here and those of Tao et al. (2010) may indicate a re-  
 561 lationship between heightened dawn sector conductance and incident solar extreme ul-  
 562 traviolet (EUV) photons, which increase the Pedersen conductance by ionizing the iono-  
 563 sphere.

## 564 5 Conclusions

565 We have outlined a novel method for deriving values of the effective Pedersen con-  
 566 ductance  $\Sigma_P^*$  of Jupiter’s ME auroral ionosphere by combining remote observations of  
 567 the Jovian ME and in-situ observations of the angular velocity, or corotation rate, of mid-  
 568 dle magnetospheric plasma. This method has been developed from the theoretical un-  
 569 derstanding of MI coupling at Jupiter, which links the field-aligned currents entering the  
 570 ionosphere, estimated from the auroral brightness measured with HST, to the motion  
 571 of middle magnetospheric plasma, calculated by moment analysis of *Galileo* PLS mea-  
 572 surements. Equivalent regions of the auroral ionosphere and equatorial magnetosphere  
 573 are found using magnetic flux equivalence mapping. The non-overlapping 288 HST ob-  
 574 servations and 6751 *Galileo* measurements used in this analysis are taken to be repre-  
 575 sentative of the time-averaged Jupiter system.

576 Combining HST-derived estimates of the field-aligned currents per radian of az-  
 577 imuth  $I_{\parallel}$  with the parameter  $I_{\parallel}/\Sigma_P^*$  derived from in-situ *Galileo* PLS measurements, we  
 578 find the effective Pedersen conductance  $\Sigma_P^*$ , reduced from the true Pedersen conductance  
 579 by a factor of  $1-k$ .  $\Sigma_P^*$  ranges between  $0.03 < \Sigma_P^* < 1.66$  mho in the north and  $0.03 < \Sigma_P^* <$   
 580  $2.40$  mho in the south, with typical values of  $\Sigma_P^* = 0.13_{-0.07}^{+0.26}$  mho and  $\Sigma_P^* = 0.16_{-0.10}^{+0.34}$   
 581 mho in the northern and southern ME, respectively. These typical values are broadly  
 582 consistent with theoretical and modeled values (Millward et al., 2002, 2005; Gérard et  
 583 al., 2020, 2021) and slightly lower than estimates based on *Juno*/UVS measurements (Wang  
 584 et al., 2021; Al Saati et al., 2022); these differences may partially be explained by sig-  
 585 nificant uncertainty in appropriate values of  $k$ , as well as by differing methods of char-  
 586 acterizing the UV emission between these studies and that presented here. Unlike these  
 587 previous studies, the distributions of  $\Sigma_P^*$  we find reveal that it varies significantly in MLT.  
 588 In calculating  $I_{\parallel}$  from HST observations in order to determine  $\Sigma_P^*$ , we additionally find  
 589 independent estimates of the field-aligned currents entering the ionosphere of  $I_{\parallel} = 9.34_{-3.54}^{+5.72}$   
 590 MA rad<sup>-1</sup> and  $I_{\parallel} = 8.61_{-3.05}^{+6.77}$  MA rad<sup>-1</sup>, corresponding to the northern and southern  
 591 ME, respectively, in quantitative agreement with recent *Juno*-based measurements (Kotsiaros  
 592 et al., 2019; Nichols & Cowley, 2022; Kamran et al., 2022) and theoretical estimates (Hill,  
 593 2001; Cowley & Bunce, 2001; Cowley et al., 2008). The distributions of field-aligned cur-  
 594 rents  $I_{\parallel}$  found here also qualitatively agree with the distribution found from multi-spacecraft  
 595 magnetometer analysis, which shows stronger field-aligned current densities near dusk  
 596 than near dawn (Lorch et al., 2020). Taking these results together, this analysis indicates  
 597 that the field-aligned currents derived from MI coupling theory, which have historically  
 598 been used to explain Jupiter’s ME, are an adequate description of the relationship be-  
 599 tween ME auroral brightness and the motion of middle magnetospheric plasma.

600 The measurement of heightened effective Pedersen conductances near MLTs of 6–  
 601 9 and 12–13 MLT is an interesting result, as these elevated conductances are approx-  
 602 imately co-located with auroral features in the ME with subcorotational motions (Rutala  
 603 et al., 2022; Radioti et al., 2008; Palmaerts et al., 2014). The results we present thus sup-  
 604 port the theory that ionospheric Pedersen conductance is key to controlling the motions  
 605 of subcorotational auroral features and are compatible with the theory that the motions  
 606 of subcorotational auroral features in the dawn sector are modulated by solar EUV ion-  
 607 ization in the auroral ionosphere (Rutala et al., 2022). We cannot, however, distinguish  
 608 between this case and the case of otherwise-increased dawn currents causing locally el-  
 609 evated conductances. Breaking the observational degeneracy between these cases should  
 610 be done with comparisons of the distributions found here to models of the field-aligned  
 611 currents flowing in the MI coupling system under varying ionospheric conductance con-  
 612 ditions.

## Appendix A Additional Two-Dimensional Distributions

The two-dimensional distributions of parameters previously discussed represent statistical averages of the large dataset used here. As such statistical averages are of limited use and difficult to interpret when presented alone, here the two-dimensional distributions of the standard deviations of the parameters and of the number of measurements used are presented. The standard deviations and numbers are provided for the auroral brightness in Figure A1 and for the corotation rate  $R_C$  in Figure A2. Only the standard deviations, not the total numbers of measurements used, are presented for the derived quantities, including: the field-aligned current per radian of azimuth  $I_{\parallel}$  in Figure A3, the field-aligned current per radian of azimuth per unit conductance  $I_{\parallel}/\Sigma_P^*$  in Figure A4, and the effective Pedersen conductance  $\Sigma_P^*$  in Figure A5. In all these distributions, the standard deviations are presented as the fractional standard deviation, or the ratio of the standard deviation to the value in the bin  $\sigma/\mu$ . The resulting distributions are therefore unitless, and the relative scale of the standard deviation can be interpreted without direct comparison to the two-dimensional distribution of the relevant parameter.

## Open Research

All Hubble Space Telescope observations used in this analysis are available at the Mikulski Archive for Space Telescopes hosted by the Space Telescope Science Institute, and have been collected into a single dataset for ease of access (Rutala, 2022). All *Galileo* PLS real-time-science data are available through the Planetary Plasma Interaction (PPI) node of the Planetary Data System (PDS) (Frank et al., 2023). This research made use of the ionosphere-magnetosphere mapping code of Vogt et al. (2011) and the internal magnetic field model of Connerney et al. (2022) as made available by Wilson et al. (2023) to allow comparison between in-situ and remote measurements, as well as the MLT-varying magnetodisk models of Vogt et al. (2011) and Ray et al. (2014). For reproducibility, intermediate data products in the form of the HST-derived ME samples and *Galileo*/PLS-derived plasma samples are catalogued at <https://doi.org/10.5281/zenodo.10563000> (Rutala et al., 2024).

## Acknowledgments

This work is based on observations with the NASA/ESA Hubble Space Telescope, obtained from the Mikulski Archive for Space Telescopes (MAST) at the Space Telescope Science Institute (STScI). STScI is operated by the Association of Universities for Research in Astronomy, Inc, under NASA contract NAS5-26555. The work presented here was primarily supported by Space Telescope Science Institute (STScI) awards HST-GO-16675.002-A and HST-GO-16989.002-A to Boston University. Additionally, M. F. Vogt was supported in part by NASA grant 80NSSC17K0777. Finally, the authors would like to thank P. Withers for valuable input on the final form of this manuscript.

## References

- Acton, C., Bachman, N., Semenov, B., & Wright, E. (2018, January). A look towards the future in the handling of space science mission geometry. *Planetary and Space Science*, *150*, 9–12. doi: 10.1016/j.pss.2017.02.013
- Allegri, F., Kurth, W. S., Elliott, S. S., Saur, J., Livadiotis, G., Nicolaou, G., ... Wilson, R. J. (2021). Electron Partial Density and Temperature Over Jupiter's Main Auroral Emission Using Juno Observations. *Journal of Geophysical Research: Space Physics*, *126*(9), e2021JA029426. Retrieved from <https://agupubs.onlinelibrary.wiley.com/doi/abs/10.1029/2021JA029426> (eprint:

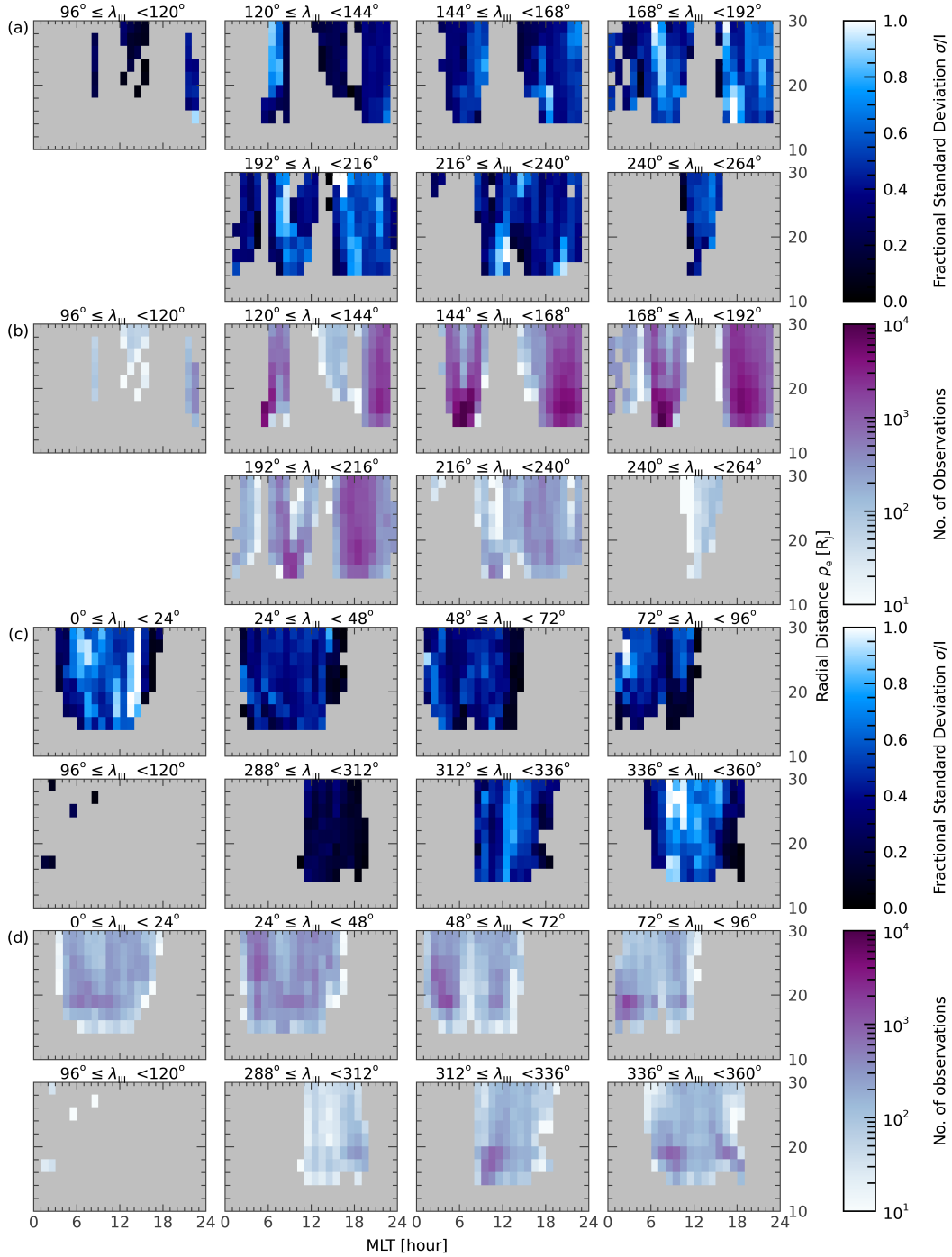


**Figure A1.** Two-dimensional distributions of the (a, c) fractional standard deviation and (b, d) number of measurements of the auroral brightness in the (a, b) northern and (c, d) southern hemispheres, as in Figure 2. Each distribution is labeled with the corresponding range of solar CMLs it spans; solar CML ranges for which there are no observations were excluded. The color of each MLT- $\rho_e$  bin corresponds to the colorbar to the right of each set of distributions. It is evident that there are more observations of the northern hemisphere than the southern hemisphere ME. Typical standard deviation values are around 0.2 – 0.4 (20 – 40% of the brightness value in that bin), with some notably high bins near 1.0; as these high-valued bins frequently have high numbers of observations, these standard deviations are not likely to be caused by a small number of outliers but instead are representative of real changes in ME auroral brightness.

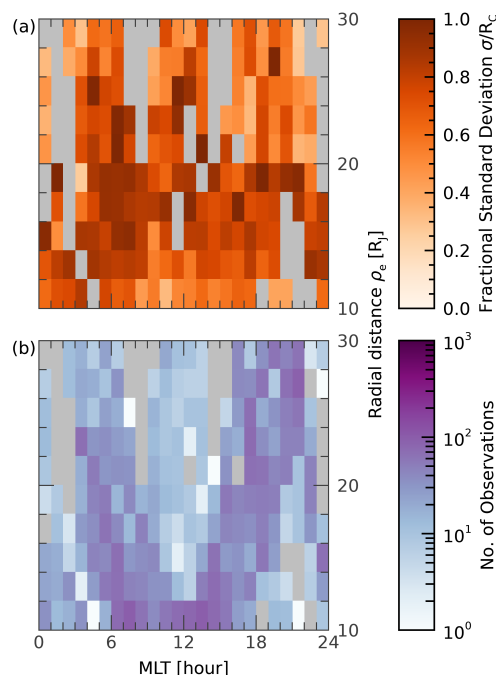


**Figure A2.** The same as Figure A1, but for (a) the fractional standard deviation and (b) the number of measurements of the magnetospheric plasma corotation rate  $R_C$ , as in Figure 4. Values of the fractional speed near 1 in bins with relatively high numbers of measurements indicates that there is a large range of measured speeds in Jupiter’s middle magnetospheric plasma.

661 <https://agupubs.onlinelibrary.wiley.com/doi/pdf/10.1029/2021JA029426> doi:  
662 <https://doi.org/10.1029/2021JA029426>

663 Al Saati, S., Clément, N., Louis, C., Blanc, M., Wang, Y., André, N., ...  
664 Mauk, B. (2022). Magnetosphere-ionosphere-thermosphere cou-  
665 pling study at jupiter based on juno’s first 30 orbits and modeling  
666 tools. *Journal of Geophysical Research: Space Physics*, *127*(10),  
667 e2022JA030586. Retrieved from <https://agupubs.onlinelibrary>  
668 [.wiley.com/doi/abs/10.1029/2022JA030586](https://doi.org/10.1029/2022JA030586) (tex.eprint:  
669 <https://agupubs.onlinelibrary.wiley.com/doi/pdf/10.1029/2022JA030586>)  
670 doi: <https://doi.org/10.1029/2022JA030586>

671 Avila, R. J., Bohlin, R., Hathi, N., Lockwood, S., Lim, P. L., & De La Peña, M.  
672 (2019, October). *SBC Absolute Flux Calibration* (Tech. Rep.). Space Tele-  
673 scope Science Institute. Retrieved from <https://www.stsci.edu/files/>  
674 [live/sites/www/files/home/hst/instrumentation/acs/documentation/](https://www.stsci.edu/files/home/hst/instrumentation/acs/documentation/instrument-science-reports-isrs/_documents/isr1905.pdf)  
675 [instrument-science-reports-isrs/\\_documents/isr1905.pdf](https://www.stsci.edu/files/home/hst/instrumentation/acs/documentation/instrument-science-reports-isrs/_documents/isr1905.pdf)

676 Bagenal, F., Wilson, R. J., Siler, S., Paterson, W. R., & Kurth, W. S. (2016, May).  
677 Survey of Galileo plasma observations in Jupiter’s plasma sheet. *Journal of*  
678 *Geophysical Research: Planets*, *121*(5), 871–894. doi: 10.1002/2016JE005009

679 Bonfond, B., Gladstone, G. R., Grodent, D., Greathouse, T. K., Versteeg, M. H.,  
680 Hue, V., ... Kurth, W. S. (2017, May). Morphology of the UV aurorae Jupiter  
681 during Juno’s first perijove observations. *Geophysical Research Letters*, *44*(10),  
682 4463–4471. doi: 10.1002/2017GL073114

683 Bonfond, B., Gustin, J., Gérard, J. C., Grodent, D., Radioti, A., Palmaerts, B., ...  
684 Tao, C. (2015, October). The far-ultraviolet main auroral emission at Jupiter  
685 - Part 1: Dawn-dusk brightness asymmetries. *Annales Geophysicae*, *33*(10),

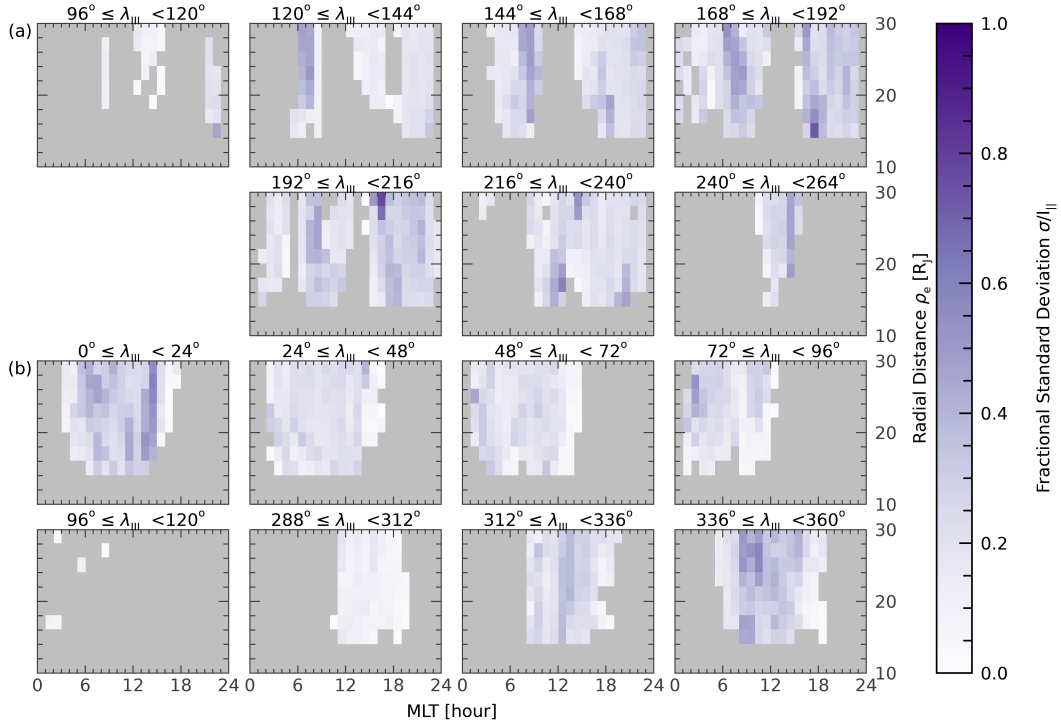


**Figure A3.** The same as Figure A1, but for the fractional standard deviation of the field-aligned currents per radian of azimuth  $I_{\parallel}$  in the (a) northern and (b) southern hemispheres, as in Figure 5. The distributions are similar to those of the fractional standard deviation in Figure A1, with high fractional standard deviations representing the true variation of the system rather than uncertainty.

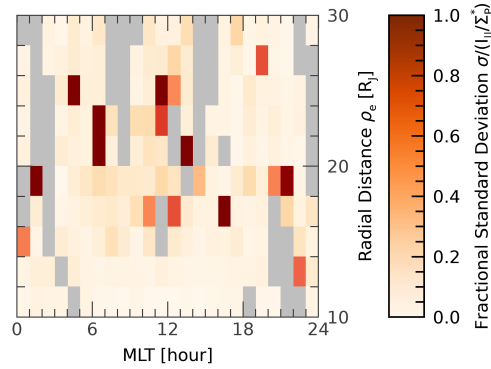


**Figure A4.** The same as Figure A2, but for the fractional standard deviation of the derived quantity  $I_{\parallel}/\Sigma_P^*$ , as in Figure 6. Compared to the fractional standard deviation shown in Figure A2, here the bins with large relative standard deviations have been made significantly more obvious owing to the conversion from  $R_C$ , which varies between 0 – 1 to  $I_{\parallel}/\Sigma_P^*$ , which varies over more than two orders of magnitude.

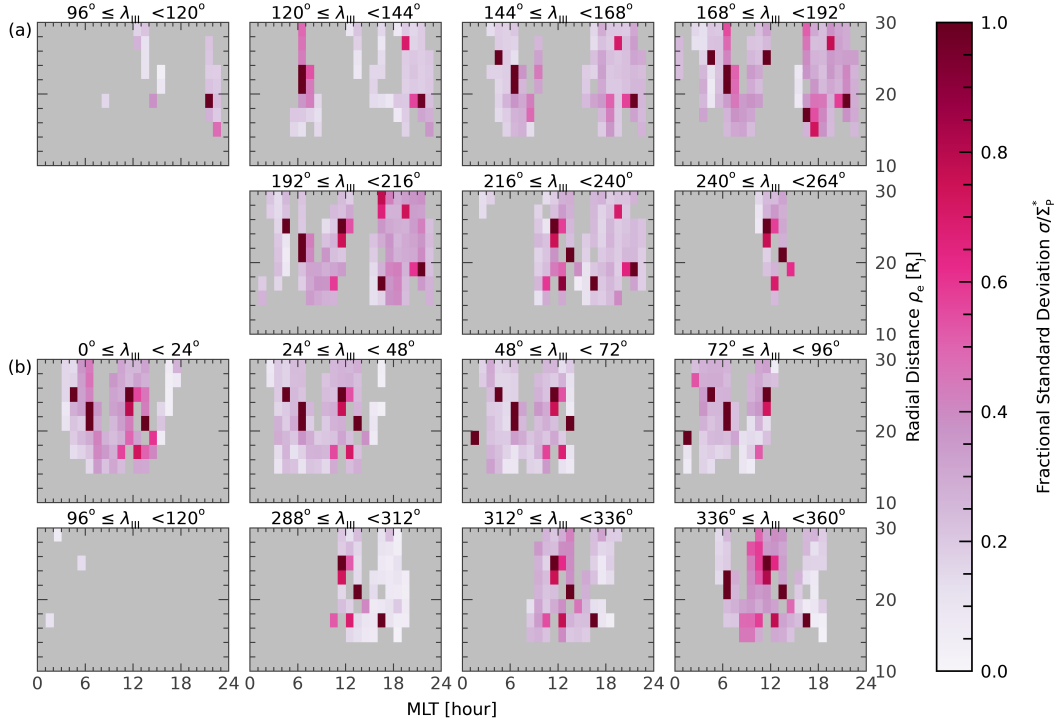


**Figure A5.** The same as in Figure A1, but for the fractional standard deviations of the effective Pedersen conductance in the (a) northern and (b) southern hemispheres, as in Figure 7. As expected, the fractional standard deviations take on aspects of both those of the field-aligned currents  $I_{||}$  (Figure A3 and that of the quantity  $I_{||}/\Sigma_P^*$  (Figure A4); as the quantity  $I_{||}/\Sigma_P^*$  does not vary with solar CML, its effects are especially evident in the form of bins with fractional standard deviations near 1. As before, these large fractional standard deviations co-occur with large numbers of observations, and thus are expected to be representative of the physical variation in the system rather than a measure of uncertainty.

- 686 1203–1209. doi: 10.5194/angeo-33-1203-2015
- 687 Bonfond, B., Yao, Z., & Grodent, D. (2020, November). Six Pieces of Evidence  
688 Against the Corotation Enforcement Theory to Explain the Main Aurora at  
689 Jupiter. *Journal of Geophysical Research: Space Physics*, *125*(11), e28152.  
690 (eprint: 2005.05938) doi: 10.1029/2020JA028152
- 691 Bonfond, B., Yao, Z. H., Gladstone, G. R., Grodent, D., Gérard, J. C., Matar, J., ...  
692 Bolton, S. J. (2021, March). Are Dawn Storms Jupiter’s Auroral Substorms?  
693 *AGU Advances*, *2*(1), e00275. doi: 10.1029/2020AV000275
- 694 Caldwell, J., Turgeon, B., & Hua, X. M. (1992, September). Hubble space tele-  
695 scope imaging of the north polar aurora on jupiter. *Science*, *257*(5076),  
696 1512–1515. (tex.adsnote: Provided by the SAO/NASA Astrophysics Data  
697 System tex.adsurl: <https://ui.adsabs.harvard.edu/abs/1992Sci...257.1512C>)  
698 doi: 10.1126/science.257.5076.1512
- 699 Chané, E., Palmaerts, B., & Radioti, A. (2018, September). Periodic shearing mo-  
700 tions in the Jovian magnetosphere causing a localized peak in the main auroral  
701 emission close to noon. *Planetary and Space Science*, *158*, 110–117. (eprint:  
702 1804.10564) doi: 10.1016/j.pss.2018.04.023
- 703 Clarke, J. T., Grodent, D., Cowley, S. W. H., Bunce, E. J., Zarka, P., Connerney,  
704 J. E. P., & Satoh, T. (2004). Jupiter’s aurora. In F. Bagenal, T. E. Dowling,  
705 & W. B. McKinnon (Eds.), *Jupiter. The Planet, Satellites and Magnetosphere*  
706 (Vol. 1, pp. 639–670).
- 707 Clarke, J. T., Nichols, J., Gérard, J.-C., Grodent, D., Hansen, K. C.,  
708 Kurth, W., ... Cecconi, B. (2009). Response of Jupiter’s and Sat-  
709 urn’s auroral activity to the solar wind. *Journal of Geophysical Re-  
710 search: Space Physics*, *114*(A5). Retrieved from [https://agupubs  
711 .onlinelibrary.wiley.com/doi/abs/10.1029/2008JA013694](https://agupubs.onlinelibrary.wiley.com/doi/abs/10.1029/2008JA013694) (eprint:  
712 <https://agupubs.onlinelibrary.wiley.com/doi/pdf/10.1029/2008JA013694>) doi:  
713 <https://doi.org/10.1029/2008JA013694>
- 714 Connerney, J. E. P., Kotsiaros, S., Oliverson, R. J., Espley, J. R., Joergensen,  
715 J. L., Joergensen, P. S., ... Levin, S. M. (2018). A New Model of  
716 Jupiter’s Magnetic Field From Juno’s First Nine Orbits. *Geophysical  
717 Research Letters*, *45*(6), 2590–2596. Retrieved from [https://agupubs  
718 .onlinelibrary.wiley.com/doi/abs/10.1002/2018GL077312](https://agupubs.onlinelibrary.wiley.com/doi/abs/10.1002/2018GL077312) (eprint:  
719 <https://agupubs.onlinelibrary.wiley.com/doi/pdf/10.1002/2018GL077312>) doi:  
720 <https://doi.org/10.1002/2018GL077312>
- 721 Connerney, J. E. P., Timmins, S., Herceg, M., & Joergensen, J. L. (2020, October).  
722 A jovian magnetodisc model for the juno era. *Journal of Geophysical Research  
723 (Space Physics)*, *125*(10), e28138. (Number: e28138 tex.adsnote: Provided by  
724 the SAO/NASA Astrophysics Data System) doi: 10.1029/2020JA028138
- 725 Connerney, J. E. P., Timmins, S., Oliverson, R. J., Espley, J. R., Joergensen, J. L.,  
726 Kotsiaros, S., ... Levin, S. M. (2022, February). A New Model of Jupiter’s  
727 Magnetic Field at the Completion of Juno’s Prime Mission. *Journal of Geo-  
728 physical Research: Planets*, *127*(2), e07055. doi: 10.1029/2021JE007055
- 729 Cowley, S. W. H., & Bunce, E. J. (2001). Origin of the main auroral oval in  
730 Jupiter’s coupled magnetosphere–ionosphere system. *Planetary and Space Sci-  
731 ence*, *49*(10), 1067–1088. Retrieved from [https://www.sciencedirect.com/  
732 science/article/pii/S0032063300001677](https://www.sciencedirect.com/science/article/pii/S0032063300001677) doi: [https://doi.org/10.1016/  
733 S0032-0633\(00\)00167-7](https://doi.org/10.1016/S0032-0633(00)00167-7)
- 734 Cowley, S. W. H., Deason, A. J., & Bunce, E. J. (2008, December). Axi-symmetric  
735 models of auroral current systems in Jupiter’s magnetosphere with pre-  
736 dictions for the Juno mission. *Annales Geophysicae*, *26*(12), 4051–4074.  
737 (tex.adsnote: Provided by the SAO/NASA Astrophysics Data System) doi:  
738 10.5194/angeo-26-4051-2008
- 739 Curran, P. A. (2014, November). Monte Carlo error analyses of Spearman’s  
740 rank test. *arXiv e-prints*, arXiv:1411.3816. (arXiv: 1411.3816 [astro-

- 741 ph.IM] tex.adsnote: Provided by the SAO/NASA Astrophysics Data System  
 742 tex.adsurl: <https://ui.adsabs.harvard.edu/abs/2014arXiv1411.3816C> tex.eid:  
 743 arXiv:1411.3816)
- 744 Frank, L., Paterson, W., & Ackerson, K. (2023). *Galileo plasma science instru-*  
 745 *ment jupiter RTS moments derived bundle*. NASA Planetary Data System.  
 746 Retrieved from [https://pds-ppi.igpp.ucla.edu/search/view/?id=pds://](https://pds-ppi.igpp.ucla.edu/search/view/?id=pds://PPI/galileo-pls-jup-derived)  
 747 [PPI/galileo-pls-jup-derived](https://pds-ppi.igpp.ucla.edu/search/view/?id=pds://PPI/galileo-pls-jup-derived) doi: doi.org/10.17189/jbaw-bm37
- 748 Gerard, J. C., & Singh, V. (1982, June). A model of energy deposition of energetic  
 749 electrons and EUV emission in the Jovian and Saturnian atmospheres and  
 750 implications. *Journal of Geophysical Research: Space Physics*, 87(A6), 4525–  
 751 4532. (tex.adsnote: Provided by the SAO/NASA Astrophysics Data System)  
 752 doi: 10.1029/JA087iA06p04525
- 753 Greathouse, T., Gladstone, R., Versteeg, M., Hue, V., Kammer, J., Giles, R., ...  
 754 Vogt, M. F. (2021, December). Local Time Dependence of Jupiter’s Polar  
 755 Auroral Emissions Observed by Juno UVS. *Journal of Geophysical Research:*  
 756 *Planets*, 126(12), e06954. doi: 10.1029/2021JE006954
- 757 Grodent, D., Bonfond, B., Gérard, J.-C., Radioti, A., Gustin, J., Clarke, J. T.,  
 758 ... Connerney, J. E. P. (2008, September). Auroral evidence of a localized  
 759 magnetic anomaly in Jupiter’s northern hemisphere. *Journal of Geophysical*  
 760 *Research: Space Physics*, 113(A9), A09201. doi: 10.1029/2008JA013185
- 761 Grodent, D., Clarke, J. T., Kim, J., Waite, J. H., & Cowley, S. W. H. (2003,  
 762 November). Jupiter’s main auroral oval observed with HST-STIS. *Jour-*  
 763 *nal of Geophysical Research: Space Physics*, 108(A11), 1389. doi: 10.1029/  
 764 2003JA009921
- 765 Grodent, D., Gérard, J.-C., Cowley, S. W. H., Bunce, E. J., & Clarke, J. T. (2005).  
 766 Variable morphology of Saturn’s southern ultraviolet aurora. *Journal of Geo-*  
 767 *physical Research: Space Physics*, 110(A7). Retrieved from [https://agupubs](https://agupubs.onlinelibrary.wiley.com/doi/abs/10.1029/2004JA010983)  
 768 [.onlinelibrary.wiley.com/doi/abs/10.1029/2004JA010983](https://agupubs.onlinelibrary.wiley.com/doi/abs/10.1029/2004JA010983) (\_eprint:  
 769 <https://agupubs.onlinelibrary.wiley.com/doi/pdf/10.1029/2004JA010983>) doi:  
 770 <https://doi.org/10.1029/2004JA010983>
- 771 Grodent, D., Waite, J., J. Hunter, & Gérard, J.-C. (2001, July). A self-consistent  
 772 model of the Jovian auroral thermal structure. *Journal of Geophysical Re-*  
 773 *search: Space Physics*, 106(A7), 12933–12952. (tex.adsnote: Provided by the  
 774 SAO/NASA Astrophysics Data System) doi: 10.1029/2000JA900129
- 775 Gustin, J., Bonfond, B., Grodent, D., & Gérard, J.-C. (2012). Conversion  
 776 from HST ACS and STIS auroral counts into brightness, precipitated  
 777 power, and radiated power for H2 giant planets. *Journal of Geophysi-*  
 778 *cal Research: Space Physics*, 117(A7). Retrieved from [https://agupubs](https://agupubs.onlinelibrary.wiley.com/doi/abs/10.1029/2012JA017607)  
 779 [.onlinelibrary.wiley.com/doi/abs/10.1029/2012JA017607](https://agupubs.onlinelibrary.wiley.com/doi/abs/10.1029/2012JA017607) (\_eprint:  
 780 <https://agupubs.onlinelibrary.wiley.com/doi/pdf/10.1029/2012JA017607>) doi:  
 781 <https://doi.org/10.1029/2012JA017607>
- 782 Gérard, J.-C., Dols, V., Prangé, R., & Paresce, F. (1994). The morphology of  
 783 the north Jovian ultraviolet aurora observed with the Hubble Space Tele-  
 784 scope. *Planetary and Space Science*, 42(11), 905–917. Retrieved from  
 785 <https://www.sciencedirect.com/science/article/pii/0032063394900515>  
 786 doi: [https://doi.org/10.1016/0032-0633\(94\)90051-5](https://doi.org/10.1016/0032-0633(94)90051-5)
- 787 Gérard, J.-C., Gkouvelis, L., Bonfond, B., Grodent, D., Gladstone, G. R.,  
 788 Hue, V., ... Blanc, M. (2020). Spatial Distribution of the Ped-  
 789 ersen Conductance in the Jovian Aurora From Juno-UVS Spec-  
 790 tral Images. *Journal of Geophysical Research: Space Physics*,  
 791 125(8), e2020JA028142. Retrieved from [https://agupubs](https://agupubs.onlinelibrary.wiley.com/doi/abs/10.1029/2020JA028142)  
 792 [.onlinelibrary.wiley.com/doi/abs/10.1029/2020JA028142](https://agupubs.onlinelibrary.wiley.com/doi/abs/10.1029/2020JA028142) (\_eprint:  
 793 <https://agupubs.onlinelibrary.wiley.com/doi/pdf/10.1029/2020JA028142>) doi:  
 794 <https://doi.org/10.1029/2020JA028142>
- 795 Gérard, J.-C., Gkouvelis, L., Bonfond, B., Grodent, D., Gladstone, G. R., Hue, V.,

- 796 ... Giles, R. S. (2021). Variability and Hemispheric Symmetry of the Ped-  
797 ersen Conductance in the Jovian Aurora. *Journal of Geophysical Research: Space Physics*, 126(4), e2020JA028949. Retrieved from [https://agupubs](https://agupubs.onlinelibrary.wiley.com/doi/abs/10.1029/2020JA028949)  
798 [.onlinelibrary.wiley.com/doi/abs/10.1029/2020JA028949](https://agupubs.onlinelibrary.wiley.com/doi/abs/10.1029/2020JA028949) (eprint:  
799 <https://agupubs.onlinelibrary.wiley.com/doi/pdf/10.1029/2020JA028949>) doi:  
800 <https://doi.org/10.1029/2020JA028949>  
801
- 802 Gérard, J. C., Grodent, D., Prange, R., Waite, J. H., Gladstone, G. R., Dols, V., ...  
803 Franke, K. A. (1994, December). A Remarkable Auroral Event on Jupiter Ob-  
804 served in the Ultraviolet with the Hubble Space Telescope. *Science*, 266(5191),  
805 1675–1678. doi: 10.1126/science.266.5191.1675
- 806 Gérard, J.-C., Grodent, D., Radioti, A., Bonfond, B., & Clarke, J. T. (2013). Hub-  
807 ble observations of Jupiter’s north–south conjugate ultraviolet aurora. *Icarus*,  
808 226(2), 1559–1567. Retrieved from [https://www.sciencedirect.com/](https://www.sciencedirect.com/science/article/pii/S0019103513003552)  
809 [science/article/pii/S0019103513003552](https://www.sciencedirect.com/science/article/pii/S0019103513003552) doi: [https://doi.org/10.1016/](https://doi.org/10.1016/j.icarus.2013.08.017)  
810 [j.icarus.2013.08.017](https://doi.org/10.1016/j.icarus.2013.08.017)
- 811 Gérard, J. C., Mura, A., Bonfond, B., Gladstone, G. R., Adriani, A., Hue, V., ...  
812 Levin, S. M. (2018, September). Concurrent ultraviolet and infrared obser-  
813 vations of the north Jovian aurora during Juno’s first perijove. *Icarus*, 312,  
814 145–156. (tex.adsnote: Provided by the SAO/NASA Astrophysics Data Sys-  
815 tem tex.adsurl: <https://ui.adsabs.harvard.edu/abs/2018Icar..312..145G>) doi:  
816 [10.1016/j.icarus.2018.04.020](https://doi.org/10.1016/j.icarus.2018.04.020)
- 817 Hill, T. W. (1979, November). Inertial limit on corotation. *Journal of Geo-*  
818 *physical Research: Space Physics*, 84(A11), 6554–6558. doi: 10.1029/  
819 [JA084iA11p06554](https://doi.org/10.1029/JA084iA11p06554)
- 820 Hill, T. W. (2001). The Jovian auroral oval. *Journal of Geophysical Research: Space Physics*, 106(A5), 8101–8107. Retrieved from [https://agupubs](https://agupubs.onlinelibrary.wiley.com/doi/abs/10.1029/2000JA000302)  
821 [.onlinelibrary.wiley.com/doi/abs/10.1029/2000JA000302](https://agupubs.onlinelibrary.wiley.com/doi/abs/10.1029/2000JA000302) (eprint:  
822 <https://agupubs.onlinelibrary.wiley.com/doi/pdf/10.1029/2000JA000302>) doi:  
823 <https://doi.org/10.1029/2000JA000302>  
824
- 825 Huang, T. S., & Hill, T. W. (1989, April). Corotation lag of the Jo-  
826 vian atmosphere, ionosphere, and magnetosphere. *Journal of Geo-*  
827 *physical Research: Space Physics*, 94(A4), 3761–3765. (tex.adsnote:  
828 Provided by the SAO/NASA Astrophysics Data System tex.adsurl:  
829 <https://ui.adsabs.harvard.edu/abs/1989JGR....94.3761H>) doi: 10.1029/  
830 [JA094iA04p03761](https://doi.org/10.1029/JA094iA04p03761)
- 831 Huscher, E., Bagenal, F., Wilson, R. J., Allegrini, F., Ebert, R. W., Valek,  
832 P. W., ... Levin, S. M. (2021). Survey of Juno Observations in  
833 Jupiter’s Plasma Disk: Density. *Journal of Geophysical Research: Space Physics*, 126(8), e2021JA029446. Retrieved from [https://agupubs](https://agupubs.onlinelibrary.wiley.com/doi/abs/10.1029/2021JA029446)  
834 [.onlinelibrary.wiley.com/doi/abs/10.1029/2021JA029446](https://agupubs.onlinelibrary.wiley.com/doi/abs/10.1029/2021JA029446) (eprint:  
835 <https://agupubs.onlinelibrary.wiley.com/doi/pdf/10.1029/2021JA029446>) doi:  
836 <https://doi.org/10.1029/2021JA029446>  
837
- 838 Kamran, A., Bunce, E. J., Cowley, S. W. H., James, M. K., Nichols, J. D., Provan,  
839 G., ... Gladstone, G. R. (2022, December). Auroral field-aligned current  
840 signatures in jupiter’s magnetosphere: Juno magnetic field observations and  
841 physical modeling. *Journal of Geophysical Research (Space Physics)*, 127(12),  
842 e2022JA030431. (tex.adsnote: Provided by the SAO/NASA Astrophysics Data  
843 System tex.adsurl: <https://ui.adsabs.harvard.edu/abs/2022JGRA..12730431K>  
844 [tex.eid: e2022JA030431](https://ui.adsabs.harvard.edu/abs/2022JGRA..12730431K)) doi: 10.1029/2022JA030431
- 845 Khurana, K. K., & Schwarzl, H. K. (2005, July). Global structure  
846 of Jupiter’s magnetospheric current sheet. *Journal of Geophys-*  
847 *ical Research: Space Physics*, 110(A7), A07227. (tex.adsnote: Pro-  
848 vided by the SAO/NASA Astrophysics Data System tex.adsurl:  
849 <https://ui.adsabs.harvard.edu/abs/2005JGRA..110.7227K> tex.eid: A07227)  
850 doi: 10.1029/2004JA010757

- 851 Kita, H., Kimura, T., Tao, C., Tsuchiya, F., Murakami, G., Yamazaki, A., ... Fuji-  
852 moto, M. (2019, December). Jovian UV Aurora's Response to the Solar Wind:  
853 Hisaki EXCEED and Juno Observations. *Journal of Geophysical Research:  
854 Space Physics*, *124*(12), 10,209–10,218. doi: 10.1029/2019JA026997
- 855 Knight, S. (1973, May). Parallel electric fields. *Planetary and Space Science*, *21*(5),  
856 741–750. doi: 10.1016/0032-0633(73)90093-7
- 857 Kotsiaros, S., Connerney, J. E. P., Clark, G., Allegrini, F., Gladstone, G. R., Kurth,  
858 W. S., ... Levin, S. M. (2019, July). Birkeland currents in Jupiter's magneto-  
859 sphere observed by the polar-orbiting Juno spacecraft. *Nature Astronomy*, *3*,  
860 904–909. doi: 10.1038/s41550-019-0819-7
- 861 Krupp, N., Lagg, A., Livi, S., Wilken, B., Woch, J., Roelof, E. C., & Williams, D. J.  
862 (2001, November). Global flows of energetic ions in Jupiter's equatorial plane:  
863 First-order approximation. *Journal of Geophysical Research: Space Physics*,  
864 *106*(A11), 26017–26032. doi: 10.1029/2000JA900138
- 865 Lorch, C. T. S., Ray, L. C., Arridge, C. S., Khurana, K. K., Martin, C. J., & Bader,  
866 A. (2020, February). Local Time Asymmetries in Jupiter's Magnetodisc Cur-  
867 rents. *Journal of Geophysical Research: Space Physics*, *125*(2). Retrieved 2022-  
868 05-18, from <https://onlinelibrary.wiley.com/doi/10.1029/2019JA027455>  
869 doi: 10.1029/2019JA027455
- 870 Mauk, B. H., Clark, G., Gladstone, G. R., Kotsiaros, S., Adriani, A., Allegrini,  
871 F., ... Rymer, A. M. (2020, March). Energetic Particles and Acceleration  
872 Regions Over Jupiter's Polar Cap and Main Aurora: A Broad Overview.  
873 *Journal of Geophysical Research: Space Physics*, *125*(3), e27699. doi:  
874 10.1029/2019JA027699
- 875 Mauk, B. H., Haggerty, D. K., Paranicas, C., Clark, G., Kollmann, P., Rymer,  
876 A. M., ... Valek, P. (2017, September). Discrete and broadband electron  
877 acceleration in Jupiter's powerful aurora. *Nature*, *549*(7670), 66–69. doi:  
878 10.1038/nature23648
- 879 Mauk, B. H., Haggerty, D. K., Paranicas, C., Clark, G., Kollmann, P., Rymer,  
880 A. M., ... Valek, P. (2018, February). Diverse Electron and Ion Acceleration  
881 Characteristics Observed Over Jupiter's Main Aurora. *Geophysical Research  
882 Letters*, *45*(3), 1277–1285. doi: 10.1002/2017GL076901
- 883 Millward, G., Miller, S., Stallard, T., Achilleos, N., & Aylward, A. D. (2005,  
884 January). On the dynamics of the jovian ionosphere and thermosphere..  
885 IV. Ion-neutral coupling. *Icarus*, *173*(1), 200–211. (tex.adsnote:  
886 Provided by the SAO/NASA Astrophysics Data System tex.adsurl:  
887 <https://ui.adsabs.harvard.edu/abs/2005Icar..173..200M>) doi: 10.1016/  
888 j.icarus.2004.07.027
- 889 Millward, G., Miller, S., Stallard, T., Aylward, A. D., & Achilleos, N. (2002). On  
890 the Dynamics of the Jovian Ionosphere and Thermosphere: III. The Modelling  
891 of Auroral Conductivity. *Icarus*, *160*(1), 95–107. Retrieved from [https://](https://www.sciencedirect.com/science/article/pii/S0019103502969514)  
892 [www.sciencedirect.com/science/article/pii/S0019103502969514](https://www.sciencedirect.com/science/article/pii/S0019103502969514) doi:  
893 <https://doi.org/10.1006/icar.2002.6951>
- 894 Nichols, J. D., Allegrini, F., Bagenal, F., Bunce, E. J., Cowley, S. W. H., Ebert,  
895 R. W., ... Yao, Z. (2020, August). An Enhancement of Jupiter's Main Auro-  
896 ral Emission and Magnetospheric Currents. *Journal of Geophysical Research:  
897 Space Physics*, *125*(8), e27904. doi: 10.1029/2020JA027904
- 898 Nichols, J. D., Badman, S. V., Bagenal, F., Bolton, S. J., Bonfond, B., Bunce,  
899 E. J., ... Yoshikawa, I. (2017, August). Response of Jupiter's auroras to  
900 conditions in the interplanetary medium as measured by the Hubble Space  
901 Telescope and Juno. *Geophysical Research Letters*, *44*(15), 7643–7652. doi:  
902 10.1002/2017GL073029
- 903 Nichols, J. D., Clarke, J. T., Gérard, J. C., Grodent, D., & Hansen, K. C. (2009,  
904 June). Variation of different components of Jupiter's auroral emission.  
905 *Journal of Geophysical Research: Space Physics*, *114*(A6), A06210. doi:

- 10.1029/2009JA014051
- 906  
907 Nichols, J. D., & Cowley, S. (2004, May). Magnetosphere-ionosphere  
908 coupling currents in Jupiter's middle magnetosphere: effect of  
909 precipitation-induced enhancement of the ionospheric Pedersen con-  
910 ductivity. *Annales Geophysicae*, *22*(5), 1799–1827. (tex.adsnote:  
911 Provided by the SAO/NASA Astrophysics Data System tex.adsurl:  
912 <https://ui.adsabs.harvard.edu/abs/2004AnGeo..22.1799N>) doi: 10.5194/  
913 angeo-22-1799-2004
- 914 Nichols, J. D., & Cowley, S. W. H. (2003, July). Magnetosphere-ionosphere coupling  
915 currents in Jupiter's middle magnetosphere: dependence on the effective iono-  
916 spheric Pedersen conductivity and iogenic plasma mass outflow rate. *Annales  
917 Geophysicae*, *21*(7), 1419–1441. doi: 10.5194/angeo-21-1419-2003
- 918 Nichols, J. D., & Cowley, S. W. H. (2005, March). Magnetosphere-ionosphere  
919 coupling currents in Jupiter's middle magnetosphere: effect of magnetosphere-  
920 ionosphere decoupling by field-aligned auroral voltages. *Annales Geophysicae*,  
921 *23*(3), 799–808. doi: 10.5194/angeo-23-799-2005
- 922 Nichols, J. D., & Cowley, S. W. H. (2022). Relation of Jupiter's Dawn-  
923 side Main Emission Intensity to Magnetospheric Currents Dur-  
924 ing the Juno Mission. *Journal of Geophysical Research: Space  
925 Physics*, *127*(1), e2021JA030040. Retrieved from [https://agupubs  
926 .onlinelibrary.wiley.com/doi/abs/10.1029/2021JA030040](https://agupubs.onlinelibrary.wiley.com/doi/abs/10.1029/2021JA030040) (\_eprint:  
927 <https://agupubs.onlinelibrary.wiley.com/doi/pdf/10.1029/2021JA030040>) doi:  
928 <https://doi.org/10.1029/2021JA030040>
- 929 Palmaerts, B., Radioti, A., Grodent, D., Chané, E., & Bonfond, B. (2014).  
930 Transient small-scale structure in the main auroral emission at  
931 Jupiter. *Journal of Geophysical Research: Space Physics*, *119*(12),  
932 9931–9938. Retrieved from [https://agupubs.onlinelibrary  
933 .wiley.com/doi/abs/10.1002/2014JA020688](https://agupubs.onlinelibrary.wiley.com/doi/abs/10.1002/2014JA020688) (\_eprint:  
934 <https://agupubs.onlinelibrary.wiley.com/doi/pdf/10.1002/2014JA020688>)  
935 doi: <https://doi.org/10.1002/2014JA020688>
- 936 Radioti, A., Gérard, J.-C., Grodent, D., Bonfond, B., Krupp, N., & Woch, J.  
937 (2008). Discontinuity in Jupiter's main auroral oval. *Journal of Geophys-  
938 ical Research: Space Physics*, *113*(A1). Retrieved from [https://agupubs  
939 .onlinelibrary.wiley.com/doi/abs/10.1029/2007JA012610](https://agupubs.onlinelibrary.wiley.com/doi/abs/10.1029/2007JA012610) (\_eprint:  
940 <https://agupubs.onlinelibrary.wiley.com/doi/pdf/10.1029/2007JA012610>) doi:  
941 <https://doi.org/10.1029/2007JA012610>
- 942 Ray, L. C., Achilleos, N. A., Vogt, M. F., & Yates, J. N. (2014). Lo-  
943 cal time variations in Jupiter's magnetosphere-ionosphere coupling  
944 system. *Journal of Geophysical Research: Space Physics*, *119*(6),  
945 4740–4751. Retrieved from [https://agupubs.onlinelibrary  
946 .wiley.com/doi/abs/10.1002/2014JA019941](https://agupubs.onlinelibrary.wiley.com/doi/abs/10.1002/2014JA019941) (\_eprint:  
947 <https://agupubs.onlinelibrary.wiley.com/doi/pdf/10.1002/2014JA019941>)  
948 doi: <https://doi.org/10.1002/2014JA019941>
- 949 Ray, L. C., Ergun, R. E., Delamere, P. A., & Bagenal, F. (2010).  
950 Magnetosphere-ionosphere coupling at Jupiter: Effect of field-aligned po-  
951 tentials on angular momentum transport. *Journal of Geophysical Re-  
952 search: Space Physics*, *115*(A9). Retrieved from [https://agupubs  
953 .onlinelibrary.wiley.com/doi/abs/10.1029/2010JA015423](https://agupubs.onlinelibrary.wiley.com/doi/abs/10.1029/2010JA015423) (\_eprint:  
954 <https://agupubs.onlinelibrary.wiley.com/doi/pdf/10.1029/2010JA015423>) doi:  
955 <https://doi.org/10.1029/2010JA015423>
- 956 Rutala, M. J. (2022). *Data for Rutala et al. 2022*. MAST. Retrieved from [https://  
957 archive.stsci.edu/doi/resolve/resolve.html?doi=10.17909/ekt0-mf55](https://archive.stsci.edu/doi/resolve/resolve.html?doi=10.17909/ekt0-mf55)  
958 doi: doi:10.17909/ekt0-mf55
- 959 Rutala, M. J., Clarke, J. T., Mullins, J. D., & Nichols, J. D. (2022, June). Illuminat-  
960 ing the Motions of Jupiter's Auroral Dawn Storms. *Journal of Geophysical Re-*

- 961 search: *Space Physics*, 127(6), e30448. doi: 10.1029/2022JA030448
- 962 Rutala, M. J., Clarke, J. T., Vogt, M. F., & Nichols, J. D. (2024, January). *Data*  
 963 *for "Variation in the Pedersen Conductance near Jupiter's Main Emission*  
 964 *Aurora: Comparison of Hubble Space Telescope and Galileo Measurements"*.  
 965 Zenodo. Retrieved from <https://doi.org/10.5281/zenodo.10563000> doi:  
 966 10.5281/zenodo.10563000
- 967 Smith, C. G. A., & Aylward, A. D. (2009, January). Coupled rotational dynam-  
 968 ics of Jupiter's thermosphere and magnetosphere. *Annales Geophysicae*, 27(1),  
 969 199–230. (tex.adsnote: Provided by the SAO/NASA Astrophysics Data System  
 970 tex.adsurl: <https://ui.adsabs.harvard.edu/abs/2009AnGeo..27..199S>) doi: 10  
 971 .5194/angeo-27-199-2009
- 972 Southwood, D. J., & Kivelson, M. G. (2001). A new perspective con-  
 973 cerning the influence of the solar wind on the Jovian magneto-  
 974 sphere. *Journal of Geophysical Research: Space Physics*, 106(A4),  
 975 6123–6130. Retrieved from <https://agupubs.onlinelibrary>  
 976 [.wiley.com/doi/abs/10.1029/2000JA000236](https://agupubs.onlinelibrary.wiley.com/doi/abs/10.1029/2000JA000236) (\_eprint:  
 977 <https://agupubs.onlinelibrary.wiley.com/doi/pdf/10.1029/2000JA000236>)  
 978 doi: <https://doi.org/10.1029/2000JA000236>
- 979 Tao, C., Fujiwara, H., & Kasaba, Y. (2009, August). Neutral wind con-  
 980 trol of the Jovian magnetosphere-ionosphere current system. *Journal of*  
 981 *Geophysical Research: Space Physics*, 114(A8), A08307. (tex.adsnote:  
 982 Provided by the SAO/NASA Astrophysics Data System tex.adsurl:  
 983 <https://ui.adsabs.harvard.edu/abs/2009JGRA..114.8307T> tex.eid: A08307)  
 984 doi: 10.1029/2008JA013966
- 985 Tao, C., Fujiwara, H., & Kasaba, Y. (2010). Jovian magnetosphere-ionosphere  
 986 current system characterized by diurnal variation of ionospheric conductance.  
 987 *Planetary and Space Science*, 58(3), 351–364. Retrieved from <https://>  
 988 [www.sciencedirect.com/science/article/pii/S003206330900316X](http://www.sciencedirect.com/science/article/pii/S003206330900316X) doi:  
 989 <https://doi.org/10.1016/j.pss.2009.10.005>
- 990 Vogt, M. F., Kivelson, M. G., Khurana, K. K., Walker, R. J., Bonfond, B., Gro-  
 991 dent, D., & Radioti, A. (2011). Improved mapping of Jupiter's au-  
 992 roral features to magnetospheric sources. *Journal of Geophysical Re-*  
 993 *search: Space Physics*, 116(A3). Retrieved from <https://agupubs>  
 994 [.onlinelibrary.wiley.com/doi/abs/10.1029/2010JA016148](https://agupubs.onlinelibrary.wiley.com/doi/abs/10.1029/2010JA016148) (\_eprint:  
 995 <https://agupubs.onlinelibrary.wiley.com/doi/pdf/10.1029/2010JA016148>) doi:  
 996 <https://doi.org/10.1029/2010JA016148>
- 997 Waite Jr., J. H., Cravens, T. E., Kozyra, J., Nagy, A. F., Atreya, S. K., & Chen,  
 998 R. H. (1983). Electron precipitation and related aeronomy of the Jovian ther-  
 999 mosphere and ionosphere. *Journal of Geophysical Research: Space Physics*,  
 1000 88(A8), 6143–6163. Retrieved from <https://agupubs.onlinelibrary>  
 1001 [.wiley.com/doi/abs/10.1029/JA088iA08p06143](https://agupubs.onlinelibrary.wiley.com/doi/abs/10.1029/JA088iA08p06143) (tex.eprint:  
 1002 <https://agupubs.onlinelibrary.wiley.com/doi/pdf/10.1029/JA088iA08p06143>)  
 1003 doi: <https://doi.org/10.1029/JA088iA08p06143>
- 1004 Walker, R. J., & Ogino, T. (2003, April). A simulation study of currents in  
 1005 the Jovian magnetosphere. *Planetary and Space Science*, 51(4-5), 295–  
 1006 307. (tex.adsnote: Provided by the SAO/NASA Astrophysics Data System  
 1007 tex.adsurl: <https://ui.adsabs.harvard.edu/abs/2003P&SS...51..295W>) doi:  
 1008 10.1016/S0032-0633(03)00018-7
- 1009 Wang, Y., Blanc, M., Louis, C., Wang, C., André, N., Adriani, A., ... Tao,  
 1010 C. (2021). A preliminary study of magnetosphere-ionosphere-  
 1011 thermosphere coupling at jupiter: Juno multi-instrument measure-  
 1012 ments and modeling tools. *Journal of Geophysical Research: Space*  
 1013 *Physics*, 126(9), e2021JA029469. Retrieved from <https://agupubs>  
 1014 [.onlinelibrary.wiley.com/doi/abs/10.1029/2021JA029469](https://agupubs.onlinelibrary.wiley.com/doi/abs/10.1029/2021JA029469) (tex.eprint:  
 1015 <https://agupubs.onlinelibrary.wiley.com/doi/pdf/10.1029/2021JA029469>) doi:

1016 <https://doi.org/10.1029/2021JA029469>  
1017 Wilson, R. J., Vogt, M. F., Provan, G., Kamran, A., James, M. K., Brennan,  
1018 M., & Cowley, S. W. H. (2023, February). Internal and external jo-  
1019 vian magnetic fields: Community code to serve the magnetospheres of the  
1020 outer planets community. *Space Science Reviews*, *219*(1), 15. (Number:  
1021 15 tex.adsnote: Provided by the SAO/NASA Astrophysics Data System  
1022 tex.adsurl: <https://ui.adsabs.harvard.edu/abs/2023SSRv..219...15W>) doi:  
1023 10.1007/s11214-023-00961-3